Important Notice

UNIVERSITY OF CALGARY

Elasto-static and -dynamic Analysis of Subsurface Fracture Phenomena

by

David Cho

A THESIS

SUBMITTED TO THE FACULTY OF GRADUATE STUDIES

IN PARTIAL FULFILMENT OF THE REQUIREMENTS FOR THE

DEGREE OF DOCTOR OF PHILOSOPHY

DEPARTMENT OF GEOSCIENCE

CALGARY, ALBERTA

MAY, 2013

Abstract

In this thesis, we investigate fracture phenomena as it pertains to unconventional resource exploration and development, specifically in tight oil and gas. We present methods for the inference of natural fracture systems and evaluate the hydraulic fracture response, especially in the vicinity of fault related features that pose a greater risk for development.

To infer the presence of natural fractures, we develop an inversion algorithm to estimate anisotropic fracture parameters from reflection seismic data. The inversion results address several shortcomings associated with conventional techniques, including a relaxed constraint on fracture orientations and the resolution of a 90° azimuthal ambiguity, providing an improved estimate of subsurface fracture parameters. In addition, we present a case study that investigates the use of isotropic analysis to infer the presence of fractures, including the use of structural attributes and elastic properties. The combined interpretation of these results revealed the lateral extent of fractures related to a structural feature that was not possible from conventional attribute analysis alone.

Furthermore, we present two case studies to evaluate the hydraulic fracture response in the vicinity of fault related features. In the first case study, we investigate the large variations observed in the hydraulic fracture response of a tight gas reservoir. The variability was hypothesized to be the result of tectonic loading that alters the mechanical properties of the rock mass prior to brittle failure, representing a pre-rupture fault. The reflectivity response of such media was discussed to infer their presence from seismic data. In addition, an effective stress model was presented to explain the changes in the stress field experienced by the rock mass. This allows us to anticipate the stimulation response and mitigate the associated risks in the vicinity of these features. In the second

case study, we present a methodology to infer fluid mobility in the stimulated zone through analysis of the attenuation response of a time-lapse seismic survey. The results obtained from the analysis were in qualitative agreement with microseismic observations and time-lapse seismic amplitude and traveltime anomalies, suggesting fluid mobility and confirming the extent of the stimulated rock volume.

Preface

This thesis investigates fracture phenomena as it pertains to unconventional resource exploration and development. It includes methods to infer the presence of natural fractures for exploration purposes and the evaluation of the hydraulic fracture response, especially in the vicinity of fault related features that pose a greater risk for development.

Chapter two contains material from a previously published manuscript:

Cho, D., and Margrave, G. F., 2012, Azimuthal AVO inversion by simulated annealing: Canadian Journal of Exploration Geophysics, **37**, no. 1, 1-7.

Permission to include this publication has been obtained from the publisher.

Two additional papers consisting of material from chapters three and four have been submitted for publication and are currently in review.

Acknowledgements

First and foremost I would like to acknowledge my thesis advisor, Dr. Gary Margrave for his support, guidance and encouragement throughout my graduate studies. He has allowed me the freedom to explore my personal interests while providing much valuable insight into the topics that make up this thesis.

In addition, I would like to acknowledge Frederik Horn, Dr. David Close, Dr. Shawn Maxwell, Craig Coulombe, Bill Goodway and Dr. Jeff Grossman, whom I have worked and collaborated with over the years. They have been a great source of inspiration and were instrumental in the development of my scientific career. Two of my physics professors, Dr. David Knudsen and Dr. Rachid Ouyed motivated me during the course of my undergraduate studies to pursue a career in physics, to which I am truly grateful. Much appreciation is also owed to the faculty, staff and students of the CREWES project, especially Dr. Kris Innanen, Dr. Larry Lines, Kevin Hall, Byron Kelly, Andrew Nicol, Jessie Arthur, Chris Bird, Faranak Mahmoudian, Peter Gagliardi, Hormoz Izadi and Steve Kim.

Finally and most importantly, I would like to thank my family and friends. Without their support, none of this would have been possible.

Dedication

To my parents.

Table of Contents

List of Tables

List of Figures and Illustrations

xiii

Epigraph

Physics is to be regarded not so much as the study of something *a priori* given, but rather as the development of methods for ordering and surveying human experience.

- Niels Bohr

Chapter One

Introduction

In 1956, Hubbert proposed that the rate of fossil fuel production for any given geographic area tends to follow a bell-shaped curve, where the production curve can be derived from past production data and an estimate of the ultimate recovery volume (Hubbert, 1956). Hubbert's original prediction for peak world oil production occurs early in the 21st century, and therefore, suggests that present production numbers should be in the stages of decline as a result of resource depletion.
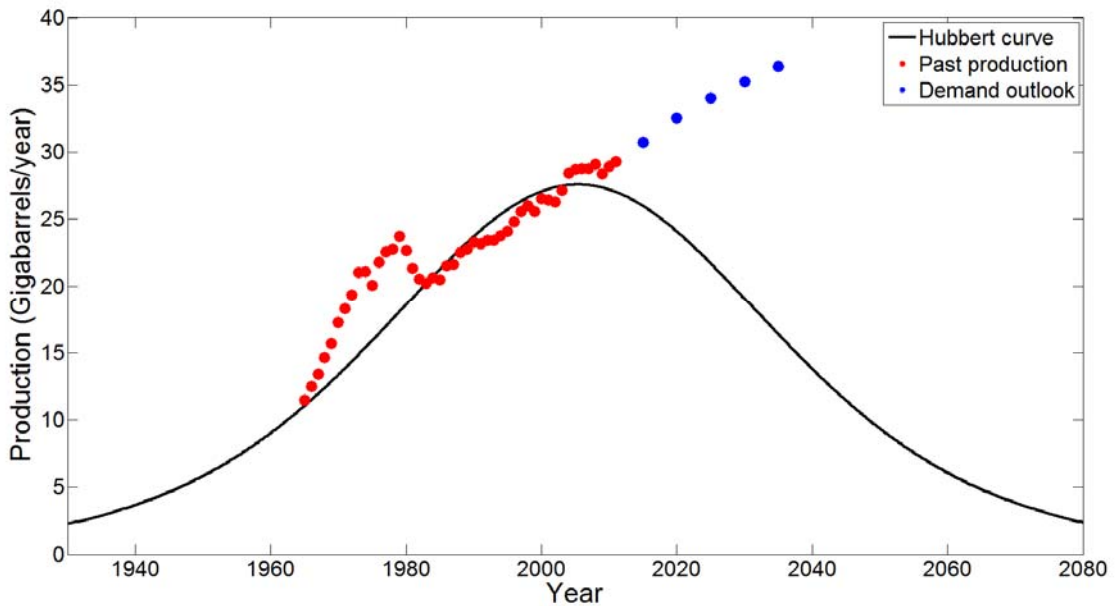
Figure 1.1. Hubbert curve (black) for world oil production derived from past production data (red) and the world oil demand outlook (blue) projected to 2035.

Using data from the BP Statistical Review of World Energy 2012 (www.bp.com), we analyze the production data to gain insight into the current state of hydrocarbon production. Figure 1.1 shows the Hubbert curve (black) for world oil production derived from past production data (red) and the world oil demand outlook (blue) projected to 2035. The peak production as predicted by Hubbert's theory occurs in the year 2006. However, the actual production numbers indicate an increase in production past the predicted peak with a demand outlook that exhibits a further increasing trend.
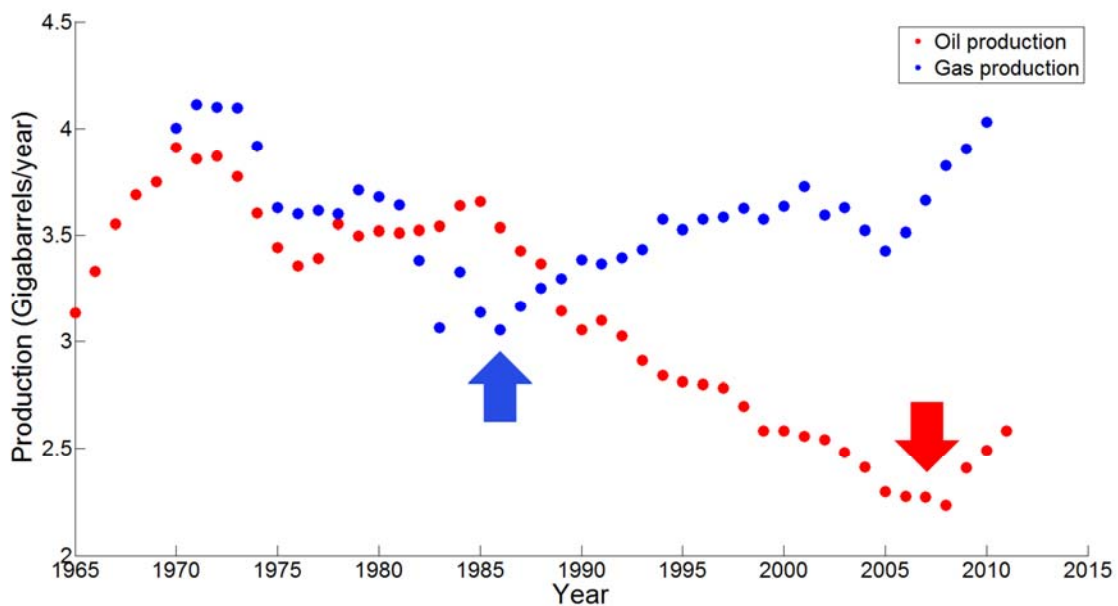
Figure 1.2. US oil and gas production trends illustrating the relationship between an increase in production numbers and events corresponding to technological advances in tight oil and gas.

Now consider the US oil and gas production trends as shown in Figure 1.2. In 1986, the first successful air drilled multiple hydraulic fracture slant well was completed in Devonian shale (Yost II et al., 1990), which sparked the shale gas revolution and marks the beginning of an increasing trend in US gas production (blue arrow in Figure 1.2).

Furthermore, these technologies were applied to tight oil and 2007 marks an increase in oil production from tight formations such as the Eagle Ford and Bakken (red arrow in Figure 1.2).

The advent of tight oil and gas has changed the landscape for energy development and is attributed to the deviation of production numbers from the Hubbert curve as illustrated in Figure 1.1. As the outlook for energy demand continues to rise, advancements in technology must also be made to unlock new resources to secure the energy supply. This increasing worldwide demand for energy presents a unique set of challenges for geoscientists to better understand the subsurface environment. In doing so, Earth resources can be harnessed in a safe and effective manner to achieve energy security and sustain economic growth.

The development of unconventional energy resources range from the extraction of hydrocarbons from tight reservoirs to harnessing geothermal energy from deep crustal rocks, both of which require a more quantitative description beyond the conventional interpretation of subsurface structure. Permeability is often a key issue in the development of unconventional energy resources. For example, the capacity for fluid flow in subsurface formations is required for hydrocarbon extraction or heat exchange in a thermal reservoir (e.g., Potter et al., 1974; Duchane and Brown, 2002). Natural fractures at all scales from microcracks to geological faults play a crucial role in the transport of fluids, and therefore must be thoroughly understood. Additionally, in low permeability formations, hydraulic fracturing is often necessary to stimulate fluid flow, where large volumes of pressurized fluids are injected into the subsurface to induce fracture generation. Although the physical mechanisms are poorly understood at present, the

prevalent paradigm is that water diffusion stimulates shear failure on multiple small pre-existing fractures and faults, creating a network of permeable flow paths (Zoback et al., 2012). As there is much controversy surrounding the subject of hydraulic fracturing, including non-containment of fractures and the rare case of earthquake (felt seismicity with moment magnitude (M) > 2) induction (e.g., Eisner et al., 2011; Holland, 2011), there exists a dire need to understand the mechanisms responsible for the process. Characterization of subsurface fractures is therefore essential for understanding permeability and for the safe and effective implementation of stimulation technologies.

The characterization of subsurface fractures requires a multi-disciplinary treatment that spans various fields in the physical sciences, most of which are firmly rooted in elasticity theory. For example, geomechanics or more specifically, rock mechanics is the branch of mechanics concerned with the response of rock to the force fields of its physical environment (Judd, 1964). Therefore, geomechanics provides the framework for evaluating the fracture and stress characteristics associated with a rock mass. In addition, seismology is the study of earthquakes and the propagation of elastic waves through the Earth. In a reflection seismic experiment, stresses imposed on the medium by the incident wavefield result in strains that excite particle motion detectable by the scattered wavefield. Subject to the assumption that linear elasticity holds, analysis of the stress and strain relationship yields the elastic stiffness parameters that characterize a medium. Seismology therefore provides the means for remote sensing of subsurface elastic properties. Therefore, geomechanics and seismology represent the elasto-static and -dynamic problems respectively that provide the necessary tools for a quantitative

4

description of subsurface fracture phenomena without a direct measurement of the mechanical properties by means of drilling or excavation.

Conventional techniques in exploration seismology were primarily concerned with the imaging of subsurface strata to identify trapping mechanisms such as anticlines and faults, from which hydrocarbon accumulation can occur. As these conventional reservoirs are depleted over time, the need to better understand the reservoir conditions was apparent in order to enhance recovery and extend the life of existing fields. Additionally, variable productivity in unconventional reservoirs has pressed for an improved understanding of reservoir heterogeneities. This has resulted in a shift towards more quantitative methods for the description of the subsurface, from which the discipline, reservoir characterization has emerged. In characterizing the reservoir, conditions including the internal and external geometry, lithology, fluid content, elastic and geomechanical properties and flow pathways must be well understood. To determine the reservoir geometry, structural attributes have proven useful from which subtle changes in reflection character can be extracted to identify features such as channel boundaries, faults, folds and stratigraphic units. In addition, amplitude variation with offset (AVO) techniques have been extremely successful in the discrimination of lithology and fluid characteristics. Moreover, inversion techniques have transformed seismic data, which are inherently measures of the interface properties, into estimates of elastic properties associated with individual rock layers. Therefore, the implementation of these methods is crucial for understanding the reservoir conditions. In this thesis, the focus is on reservoir characterization with an emphasis on the description of fractured systems.

1.1 Overview of conventional seismic fracture characterization techniques

Seismic methods for fracture characterization can be generalized to include azimuthal and non-azimuthal techniques, where the two are based upon different concepts and underlying assumptions. Azimuthal techniques attempt to exploit the anisotropic nature of fractured media to make direct measurements of azimuthal variations in the seismic response, from which fracture parameters can be estimated. Alternatively, non-azimuthal techniques typically invoke assumptions regarding the relationship between structural deformation and the formation of fractures to infer their presence. Various benefits and pitfalls are associated with these general methods and will facilitate or hinder their usefulness. In the following, we provide a brief description of azimuthal and non-azimuthal techniques and discuss some areas where improvements can be made.

1.1.1 Azimuthal techniques

Direct methods for fracture detection typically require an azimuthal analysis of the seismic wavefield. Such analysis is motivated by the theoretical observation that aligned fractures introduce anisotropy in the medium that manifests as azimuthal variations in the seismic response. An observable effect includes the variation of reflection amplitudes with azimuth from which fracture parameters can be estimated (e.g., Rüger and Tsvankin, 1997; Rüger, 1998; Jenner, 2002). Methodologies that make use of these seismic signatures are referred to as amplitude variation with azimuth (AVAZ) techniques. These methods are therefore direct in the sense that a measureable physical response of fractures is detected.

AVAZ techniques typically invoke the assumption of a transversely isotropic medium with a horizontal axis of rotational symmetry (HTI). These methods are based upon the work of Rüger (1998) where approximate scattering coefficients were derived for an interface separating two HTI layers with the same symmetry axis azimuth. The result of such azimuthal amplitude analysis typically yields the fracture orientation and a parameter that relates to the fracture intensity such as the anisotropic gradient, which controls the azimuthal variations in the reflection response (e.g., Jenner, 2002).

Various limitations are associated with these methodologies. Firstly, the analysis is performed on reflection amplitudes. Therefore, the output is an interface property whereas fracture parameters are inherently a property of individual layers. In addition, Rüger's formulation of the scattering coefficients is restricted to an invariant symmetry axis azimuth above and below the reflecting interface or must have an isotropic overburden, and thus limits its applicability in more general cases. Furthermore, an inherent non-linearity is present when solving for the fracture orientation using this approach, resulting in a 90° ambiguity and consequently a non-unique solution (Rüger, 1998). These issues present various challenges in the interpretation of the estimated fracture parameters and can lead to erroneous results and uncertain outcomes. Therefore, improvements must be made to alleviate the shortcomings associated with conventional AVAZ techniques.

1.1.2 Non-azimuthal techniques

Non-azimuthal techniques for fracture characterization are typically based on attribute analysis of the post-stack seismic image and target fractures that are related to structural

deformation. Therefore, attributes that are sensitive to the structure of the seismic image are used to infer the presence of the associated fracture systems. These include attributes such as dip magnitude and azimuth, coherence and curvature from which disruptions in reflector continuity can be extracted from the seismic image. These discontinuity-attributes highlight events corresponding to faults and folds associated with deformed strata where fractures can form (e.g., Chopra and Marfurt, 2007). Although it is well established that fractures are correlated to structure, attribute analysis is an indirect method, where a physical response of fractures is not measured and their presence in the vicinity of structural features are merely inferred. Furthermore, fractures can exist that are not necessarily accompanied by structural changes detectable at the seismic scale. Therefore, these fracture systems cannot be inferred from attribute analysis and require alternative methodologies to detect their presence.

1.2 Overview of hydraulic fracturing for unconventional resource development

The extraction of hydrocarbons from unconventional reservoirs was predominantly an engineering focus in the early stages of development. The low permeability rock required engineering disciplines to develop solutions for extended reach laterals and hydraulic fracture treatments to achieve economic recovery rates, where these processes attempt to maximize reservoir contact through multi-stage injection of pressurized fluids to create induced fracture systems and stimulate the mobility of reservoir fluids.

Microseismic (M < 2) techniques were first introduced to the field of hydraulic fracturing to monitor the microseisms induced by rock failure. This information was used primarily to determine the extent of fracture propagation through event locations where it

was conjectured that the microseismic event cloud provided an estimate of the stimulated rock volume (SRV) (e.g., Warpinski et al., 2012). Microseismic imaging of hydraulic fracture treatments has shown that the fracture complexity is highly variable in certain settings, where fracture behavior ranging from simple planar fractures to complex fracture networks were observed along the length of a single horizontal well (Cipolla et al., 2010). This could be the result of changing lithological conditions or the presence of natural fractures. However, the most extreme cases of variability are typically associated with fault related features that are accompanied by large variations in the in-situ stress field. These features are of greater concern as their hydraulic fracture behavior is less predictable. Moreover, elevated fluid pressures in the vicinity of sufficiently large faults near the state of critical stress could induce earthquakes (Shemeta et al., 2012). Therefore, faults must be identified and their physical mechanisms understood to mitigate the associated risks. For these reasons, seismic techniques have been applied extensively in recent years to characterize unconventional reservoirs to better understand the subsurface heterogeneity in an attempt to anticipate the hydraulic fracture response. Furthermore, a shift towards more advanced analysis of the microseismicity beyond event locations is being applied to further understand the hydraulic fracturing process. This allows for the reservoir conditions estimated from seismic data to be corroborated by direct measurements of the stimulation process offered by the induced microseismicity, therefore providing the necessary means to characterize the hydraulic fracture response.

1.3 Thesis outline

The objective of this thesis is to investigate subsurface fracture phenomena for the purpose of advancing the techniques associated with unconventional resource exploration and development, specifically tight oil and gas. It includes methods to infer the presence of natural fractures through the use of seismic sounding techniques and the evaluation of the hydraulic fracture response, especially in the vicinity of fault related features through integration of seismic and microseismic analysis.

To infer the presence of natural fractures, we investigate both azimuthal and non-azimuthal techniques for their ability to delineate the associated fracture systems.

In chapter two, we discuss a technique for fracture characterization using azimuthal analysis, where we present a forward modeling and inversion strategy to directly estimate fracture parameters from reflection seismic data. To address the limitations associated with conventional azimuthal techniques, we use a more general form of the scattering coefficients to represent lower symmetry systems for a more general description of fractured media. We subsequently perform an inversion on synthetic data to estimate the elastic and fracture properties associated with individual layers.

In chapter three, we present a methodology through a case study illustrating the use of isotropic analysis for fracture inference. The presence of fractures related to seismic scale structural changes were inferred from attribute analysis of the post-stack seismic image. Additionally, fractures not directly correlated to such structural changes were inferred through changes in effective elastic properties as a result of fracturing, where the analysis was carried out through consideration of anisotropic fracture models. We subsequently

make a combined interpretation of the structural attributes and elastic properties to reduce the overall uncertainty associated with conventional attribute analysis alone.

To investigate the hydraulic fracture response in the vicinity of fault related features, we present two case studies illustrating the use of seismic and microseismic analysis to characterize their behavior. Specifically, we investigate the reservoir conditions that are identifiable through seismic analysis and evaluate the corresponding hydraulic fracture response through microseismic observations.

In chapter four, we present the first case study where we investigate the variability in the hydraulic fracture response associated with the stimulation of a tight gas reservoir, where failure occurs under two different stress regimes over a relatively small distance. The variability was hypothesized to be the result of tectonic loading that alters the mechanical properties of the rock mass prior to brittle failure, representing a pre-rupture fault. We discuss methods for the detection of these features and present a micromechanical model to explain the changes in the stress field experienced by the rock mass.

In chapter five, we present the second case study where we investigate the use of time-lapse (4D) seismic data to characterize fluid mobility in the stimulated zone and map the SRV. The microseismic monitoring results demonstrated a diversion of hydraulic fracture energy to a specific portion of the reservoir for stages in close proximity to a fault identified from seismic data, suggesting the existence of permeable pathways in the reservoir that influenced the stimulation program. To validate the existence of the permeable fault, we perform a spectral analysis to evaluate the attenuation response,

which was hypothesized to be the result of squirt flow effects that can be used to infer the mobility of fluids and hence, the permeability in the reservoir.

In chapter six, we provide a summary of the material presented and outline the contributions that were made in this thesis.

Finally, in chapter seven, we discuss future directions for fracture characterization and the investigation of the hydraulic fracturing process. Although incremental steps forward have been made in these subjects, many questions still remain unanswered. We discuss some of the outstanding issues and suggest possible research directions to advance our understanding of this critical subject.

Chapter Two

Azimuthal AVO inversion

2.1 Introduction

To address the limitations associated with conventional AVAZ techniques as discussed in §1.1.1, we develop an azimuthal AVO inversion algorithm to estimate subsurface fracture parameters from reflection seismic data as in Downton and Roure (2010). We begin with a discussion on the form of the elastic stiffness matrix corresponding to a medium with arbitrary fracture orientations. Subsequently, we examine the seismic reflection response from an interface separating such media. Finally, the inversion is presented as an optimization problem where we demonstrate its utility using synthetic data.

2.2 Coordinate transformations

Consider a transversely isotropic (TI) medium where the anisotropy is due to the presence of an aligned fracture system, and has an axis of rotational symmetry normal to the fracture plane. Here, we generalize the HTI model as discussed in §1.1.1, where the symmetry axis can deviate from the horizontal plane to allow for arbitrary fracture orientations. In addition, we define the natural coordinate system of a TI medium as one where the symmetry axis is coincident with one of the coordinate axes. Figure 2.1 illustrates the TI model where the symmetry axis coincides with the x_1 axis, and represents the case of vertical fractures in the x_2-x_3 plane.
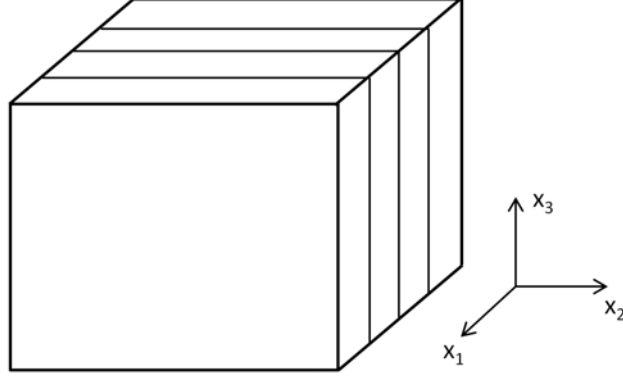
Figure 2.1. TI medium in its natural coordinate system where the symmetry axis coincides with the x_1 axis, representing a medium with aligned vertical fractures.

Here, we use the Voigt notation $A_{\alpha\beta}$ rather than the tensor notation a_{ijkl} for the density normalized elastic stiffness parameters, with α and β running from 1 to 6 and i, j, k and l running from 1 to 3. From here on in, the density normalized elastic stiffness parameters are referred to as the elastic stiffness parameters. The elastic stiffness matrix for the configuration in Figure 2.1 is given by

$$\underline{\underline{A^n}} = \begin{bmatrix} A_{11}^n & A_{12}^n & A_{13}^n & 0 & 0 & 0 \\ A_{12}^n & A_{22}^n & A_{23}^n & 0 & 0 & 0 \\ A_{13}^n & A_{23}^n & A_{33}^n & 0 & 0 & 0 \\ 0 & 0 & 0 & A_{44}^n & 0 & 0 \\ 0 & 0 & 0 & 0 & A_{55}^n & 0 \\ 0 & 0 & 0 & 0 & 0 & A_{66}^n \end{bmatrix}, \tag{2.1}$$

where the following symmetry relations are satisfied:

$$A_{33}^n = A_{22}^n, \quad A_{55}^n = A_{66}^n, \quad A_{13}^n = A_{12}^n, \quad A_{23}^n = A_{33}^n - 2A_{44}^n. \tag{2.2}$$

The superscript n denotes the elastic stiffness parameters are in its natural coordinate system. Since the elastic stiffness matrix is symmetric, equation 2.1 consists of nine non-vanishing components of the elastic stiffness parameters where five are independent as

14

governed by the relations in equation 2.2. We note that the conditions in equations 2.1 and 2.2 are only applicable if the reference coordinate system coincides with the natural coordinate system.

Let us now investigate the effect of a reference coordinate system that deviates from the natural coordinate system, representing the influence of arbitrary fracture orientations. Here, we employ a matrix transformation technique proposed by Bond (1943). The corresponding result for the rotation of the elastic stiffness matrix is given by

$$\underline{\underline{A}} = \underline{\underline{M}}\,\underline{\underline{A}}^{n}\,\underline{\underline{M}}^{T},$$

(2.3)

where $\underline{\underline{A}}$ represents the rotated elastic stiffness matrix and $\underline{\underline{M}}$ represents the Bond transformation matrix (see Auld, 1990). In the following, we investigate the effect of a coordinate rotation about the x_2 and x_3 axes, which represent the two Euler angles required to uniquely orient a TI medium in three-space. The third angle is not required due to the rotational invariance of a TI medium about the symmetry axis.

2.2.1 Coordinate rotation about the x_2 axis

Consider a rotation of the coordinate system about the x_2 axis by an angle ξ as in Figure 2.2. This scenario represents the case of dipping fractures.
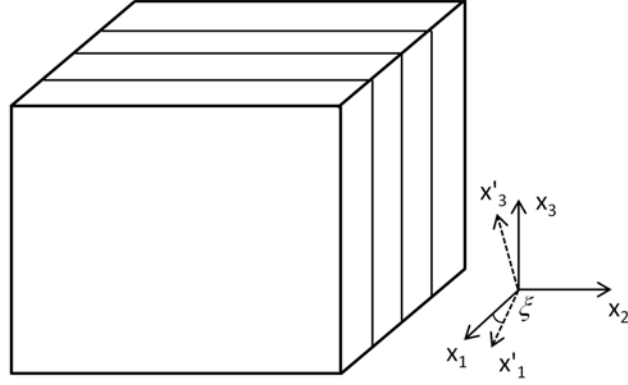
Figure 2.2. TI medium under a coordinate rotation about the x_2 axis by an angle ξ, representing the case of dipping fractures.

The corresponding Bond transformation matrix is given by

$$\underline{\underline{M}}(\xi) = \begin{bmatrix} \cos^2\xi & 0 & \sin^2\xi & 0 & -\sin 2\xi & 0 \\ 0 & 1 & 0 & 0 & 0 & 0 \\ \sin^2\xi & 0 & \cos^2\xi & 0 & \sin 2\xi & 0 \\ 0 & 0 & 0 & \cos\xi & 0 & \sin\xi \\ \dfrac{\sin 2\xi}{2} & 0 & -\dfrac{\sin 2\xi}{2} & 0 & \cos 2\xi & 0 \\ 0 & 0 & 0 & -\sin\xi & 0 & \cos\xi \end{bmatrix}, \tag{2.4}$$

and the resulting elastic stiffness matrix in the rotated coordinate system takes the form

$$\underline{\underline{A}}(\xi) = \begin{bmatrix} A_{11}(\xi) & A_{12}(\xi) & A_{13}(\xi) & 0 & A_{15}(\xi) & 0 \\ A_{12}(\xi) & A_{22}(\xi) & A_{23}(\xi) & 0 & A_{25}(\xi) & 0 \\ A_{13}(\xi) & A_{23}(\xi) & A_{33}(\xi) & 0 & A_{35}(\xi) & 0 \\ 0 & 0 & 0 & A_{44}(\xi) & 0 & A_{46}(\xi) \\ A_{15}(\xi) & A_{25}(\xi) & A_{35}(\xi) & 0 & A_{55}(\xi) & 0 \\ 0 & 0 & 0 & A_{46}(\xi) & 0 & A_{66}(\xi) \end{bmatrix}. \tag{2.5}$$

Note the appearance of A_{15}, A_{25}, A_{35} and A_{46}. The non-vanishing components of the elastic stiffness matrix now consist of 13 parameters.

2.2.2 Coordinate rotation about the x_3 axis

Next consider a rotation of the coordinate system about the x_3 axis by an angle ψ as in

Figure 2.3. This scenario represents the case of an unknown symmetry axis azimuth.
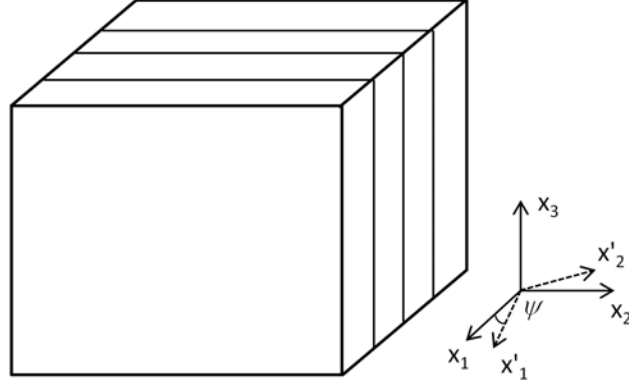
Figure 2.3. TI medium under a coordinate rotation about the x_3 axis by an angle ψ, representing the case of an unknown symmetry axis azimuth.

The corresponding Bond transformation matrix is given by

$$
\underline{\underline{M}}(\psi) =
\begin{bmatrix}
\cos^2\psi & \sin^2\psi & 0 & 0 & 0 & \sin 2\psi \\
\sin^2\psi & \cos^2\psi & 0 & 0 & 0 & -\sin 2\psi \\
0 & 0 & 1 & 0 & 0 & 0 \\
0 & 0 & 0 & \cos\psi & -\sin\psi & 0 \\
0 & 0 & 0 & \sin\psi & \cos\psi & 0 \\
-\dfrac{\sin 2\psi}{2} & \dfrac{\sin 2\psi}{2} & 0 & 0 & 0 & \cos 2\psi
\end{bmatrix},
\qquad (2.6)
$$

and the resulting elastic stiffness matrix in the rotated coordinate system takes the form

$$
\underline{\underline{A}}(\psi) =
\begin{bmatrix}
A_{11}(\psi) & A_{12}(\psi) & A_{13}(\psi) & 0 & 0 & A_{16}(\psi) \\
A_{12}(\psi) & A_{22}(\psi) & A_{23}(\psi) & 0 & 0 & A_{26}(\psi) \\
A_{13}(\psi) & A_{23}(\psi) & A_{33}(\psi) & 0 & 0 & A_{36}(\psi) \\
0 & 0 & 0 & A_{44}(\psi) & A_{45}(\psi) & 0 \\
0 & 0 & 0 & A_{45}(\psi) & A_{55}(\psi) & 0 \\
A_{16}(\psi) & A_{26}(\psi) & A_{36}(\psi) & 0 & 0 & A_{66}(\psi)
\end{bmatrix}.
\qquad (2.7)
$$

17

Note the appearance of A_{16}, A_{26}, A_{36} and A_{45}. As in the case of a rotation about the x_2 axis, the non-vanishing components of the elastic stiffness matrix now consist of 13 parameters.

The elastic stiffness matrix corresponding to one set of aligned fractures in the rotated frame consists of various combinations of sinusoidal functions and the elastic stiffness parameters in its natural coordinate system, where its form is dependent on the nature of the rotation. Therefore, no simple symmetries can be invoked once the reference coordinate system deviates from the natural coordinate system and each elastic stiffness parameter in the rotated frame must be treated as an independent parameter.

2.3 Reflection coefficients for weakly anisotropic TI media

Approximate scattering coefficients have been derived by various authors using perturbation techniques (e.g., Rüger, 1998; Vavryčuk and Pšenčík, 1998), where the objective was to obtain an approximate solution for a problem which cannot be solved exactly. This was achieved through the addition of "small" perturbative terms to the description of a similar exactly solvable problem. In the case of approximate reflection coefficients in anisotropic media, the perturbations represent the anisotropic deviation from a solvable isotropic background. The "small" perturbations therefore dictate a weak contrast interface separating two weakly anisotropic media. However, according to Thomsen (1993), this condition is valid for most reflecting interfaces and therefore the assumption of a weak contrast interface is appropriate.

In the following, we investigate two scenarios for the reflection of P-waves from an interface separating two homogeneous TI half-spaces. The first model was discussed in

Rüger (1998) where the upper and lower TI half-spaces are in its natural coordinate system and have the same symmetry axis azimuth and no fracture dip above and below the interface. The second is a more generic scenario where the upper and lower TI half-spaces have an arbitrary symmetry axis azimuth and fracture dip above and below the interface. Figure 2.4 illustrates the two scenarios.
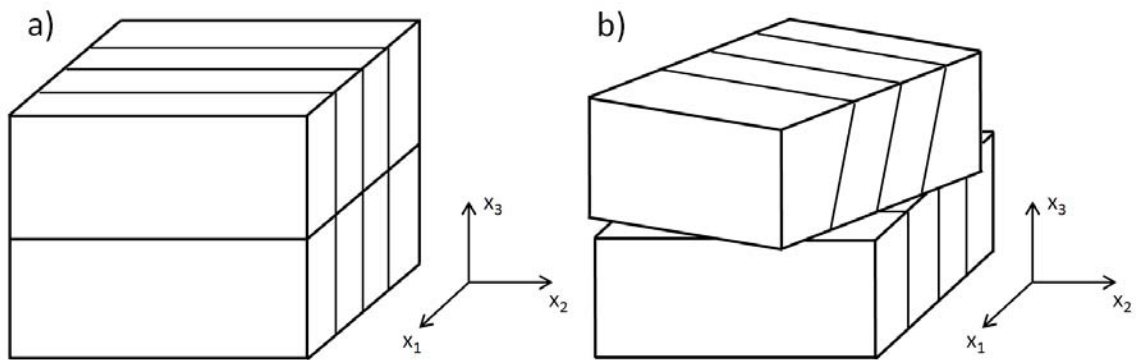
Figure 2.4. a) A TI/TI model in its natural coordinate system with the same symmetry axis azimuth and no fracture dip above and below the interface and b) a TI/TI model with an arbitrary symmetry axis azimuth and fracture dip above and below the interface.

2.3.1 TI/TI interface with the same symmetry axis azimuth and no fracture dip

For the case of a TI/TI model with the same symmetry axis azimuth and no fracture dip above and below the interface (Figure 2.4a), the P-wave reflection coefficient in its natural coordinate system is given by (Rüger, 1998)

$$R_{pp}(\theta,\phi) = \frac{1}{2}\frac{\Delta Z}{\overline{Z}} + \frac{1}{2}\left[\frac{\Delta\alpha}{\overline{\alpha}} - \left(\frac{2\overline{\beta}}{\overline{\alpha}}\right)^2\frac{\Delta G}{\overline{G}}\right.$$

$$+\left(\Delta\left(\frac{(A_{13}^n+A_{55}^n)^2-(A_{33}^n+A_{55}^n)^2}{2A_{33}^n(A_{33}^n+A_{55}^n)}\right)+2\left(\frac{2\overline{\beta}}{\overline{\alpha}}\right)^2\Delta\left(\frac{(A_{44}^n-A_{66}^n)}{2A_{66}^n}\right)\right)\cos^2\phi\left.\right]\sin^2\theta$$

$$+\frac{1}{2}\left[\frac{\Delta\alpha}{\overline{\alpha}} + \Delta\left(\frac{(A_{11}^n-A_{33}^n)}{2A_{33}^n}\right)\cos^4\phi\right.$$

$$+\Delta\left(\frac{(A_{13}^n+A_{55}^n)^2-(A_{33}^n+A_{55}^n)^2}{2A_{33}^n(A_{33}^n+A_{55}^n)}\right)\sin^2\phi\cos^2\phi\left.\right]\sin^2\theta\tan^2\theta$$

, (2.8)

where α and β are the P- and S-wave velocities respectively, $Z=\rho\alpha$ is the acoustic impedance, $G=\rho\beta^2$ is the shear modulus, ρ is the density, θ is the average angle of incidence and ϕ is the measurement azimuth. The bar represents an averaging of the values (e.g., $\bar{u}=\frac{1}{2}[u_1+u_2]$) and Δ represents a difference of the values (e.g., $\Delta u=u_2-u_1$) above and below the reflecting interface. Equation 2.8 corresponds exactly to equation 2.5 of Rüger (1998) with the exception that the elastic stiffness parameters were used instead of anisotropy parameters.

If the symmetry axis azimuth is unknown, the measurement azimuth ϕ is expressed as the difference between the azimuthal direction of the kth observed azimuth and the direction of the symmetry axis ϕ_{sym} (Rüger, 1998). The AVO gradient term in equation 2.8 is then defined as

$$B(\phi_k) = B^{iso} + B^{ani}\cos^2(\phi_k - \phi_{sym}),$$ (2.9)

with

$$B^{iso} = \frac{1}{2}\left[\frac{\Delta\alpha}{\overline{\alpha}} - \left(\frac{2\overline{\beta}}{\overline{\alpha}}\right)^2\frac{\Delta G}{\overline{G}}\right]$$ (2.10)

and

$$B^{ani} = \frac{1}{2}\left[\Delta\left(\frac{(A_{13}^n + A_{55}^n)^2 - (A_{33}^n + A_{55}^n)^2}{2A_{33}^n(A_{33}^n + A_{55}^n)}\right) + 2\left(\frac{2\overline{\beta}}{\overline{\alpha}}\right)^2 \Delta\left(\frac{(A_{44}^n - A_{66}^n)}{2A_{66}^n}\right)\right]. \quad (2.11)$$

Equation 2.9 can be used to determine the symmetry axis azimuth by solving for ϕ_{sym}. However, due to the non-linearity of equation 2.9, the solution for ϕ_{sym} is non-unique and yields two possible directions orthogonal to one another (Rüger, 1998). In addition, since the symmetry axis azimuth above and below the reflecting interface must be the same, for a multi-layered Earth, this implies an invariant fracture orientation with depth. To overcome this issue, numerous authors have imposed the condition of an isotropic overburden. The above scenarios however, pose an unrealistic constraint. Therefore, a more general TI reflection model is required for a more accurate description.

2.3.2 TI/TI interface with an arbitrary symmetry axis azimuth and fracture dip

For a more general description of the fractured media reflection problem, a TI/TI model with an arbitrary symmetry axis azimuth and fracture dip above and below the interface is considered (Figure 2.4b). As discussed above, a TI medium not in its natural coordinate system must be regarded as an anisotropic medium with non-vanishing elastic stiffness parameters as dictated by the coordinate transformations.

Vavryčuk and Pšenčík (1998) derived P-wave reflection coefficients for a weak contrast interface separating two weakly but arbitrarily anisotropic media. As a result of the perturbative derivation, the formula depends on the choice of parameters (P- and S-wave velocities) used for the isotropic background. A discussion of the effects for various background velocities can be found in Pšenčík and Martins (2001). Here, the background

P- and S-wave velocities were chosen to be $\alpha^2 = A_{33}$ and $\beta^2 = A_{44}$ respectively. These are the vertical P-wave velocity and the vertical S-wave velocity with a polarization in the x_2-x_3 plane. The P-wave reflection coefficient is then given by

$$R_{PP}(\theta,\phi) = R_{PP}^{iso}(\theta) + \frac{1}{2}\left[\Delta\left(\frac{A_{23} + 2A_{44} - A_{33}}{A_{33}}\right)\sin^2\phi\right.$$

$$+\left(\Delta\left(\frac{A_{13} + 2A_{55} - A_{33}}{A_{33}}\right) - 8\Delta\left(\frac{A_{55} - A_{44}}{2A_{33}}\right)\right)\cos^2\phi$$

$$\left. +2\left(\Delta\left(\frac{A_{36} - A_{45}}{A_{33}}\right) - 4\Delta\left(\frac{A_{45}}{A_{33}}\right)\right)\cos\phi\sin\phi\right]\sin^2\theta$$

$$+\frac{1}{2}\left[\Delta\left(\frac{A_{11} - A_{33}}{2A_{33}}\right)\cos^4\phi + \Delta\left(\frac{A_{22} - A_{33}}{2A_{33}}\right)\sin^4\phi\right.$$

$$+\Delta\left(\frac{A_{12} + 2A_{66} - A_{33}}{A_{33}}\right)\cos^2\phi\sin^2\phi + 2\Delta\left(\frac{A_{16}}{A_{33}}\right)\cos^3\phi\sin\phi$$

$$\left. +2\Delta\left(\frac{A_{26}}{A_{33}}\right)\sin^3\phi\cos\phi\right]\sin^2\theta\tan^2\theta \qquad , \qquad (2.12)$$

where

$$R_{PP}^{iso}(\theta) = \frac{1}{2}\frac{\Delta Z}{\overline{Z}} + \frac{1}{2}\left[\frac{\Delta\alpha}{\overline{\alpha}} - \left(\frac{2\overline{\beta}}{\overline{\alpha}}\right)^2\frac{\Delta G}{\overline{G}}\right]\sin^2\theta + \frac{1}{2}\frac{\Delta\alpha}{\overline{\alpha}}\sin^2\theta\tan^2\theta . \qquad (2.13)$$

Equation 2.12 consists of an isotropic term with the addition of a perturbation term to account for anisotropy. The isotropic term given by equation 2.13 is the well-known Aki and Richards (1980) approximate AVO equation for P-wave reflections. The anisotropic correction term consists of various combinations of 13 elastic stiffness parameters called weak anisotropy parameters. Note that the reflection coefficient does not depend on elastic parameters A_{14}, A_{15}, A_{24}, A_{25}, A_{34}, A_{35}, A_{46} and A_{56}. This is a direct consequence of the derivation for a surface acquisition geometry and horizontal reflectors where the P-

waves are unable to sample the medium in the directions necessary to detect certain components of the elastic stiffness matrix. Therefore, these parameters can never be recovered from a P-wave reflection experiment (Vavryčuk and Pšenčík, 1998). It is interesting to note that the non-vanishing elastic stiffness parameters in equation 2.12 take the form of a monoclinic (with a plane of mirror symmetry in the x_1-x_2 plane) crystal symmetry. It follows that the most general anisotropic medium that can be fully characterized by a P-wave reflection experiment is monoclinic.

To illustrate the effect of P-wave reflections as a result of arbitrary fracture orientations, equation 2.12 was used to calculate the reflection coefficients for three TI/TI models with various fracture geometries. To do this, a transformation from the natural coordinate system to the acquisition coordinates must be performed prior to the calculation of the reflection coefficients. The first model contains vertical fractures in its natural coordinate system with a similar symmetry axis azimuth above and below the reflecting interface, representing the Rüger (1998) model. The second model contains a 60 degree azimuthal rotation in the upper medium relative to the first model, representing an unknown symmetry axis azimuth. The third model contains a 60 degree azimuthal rotation in the upper medium and a 20 degree dip rotation in the lower medium relative to the first model. The reflection coefficients for the three scenarios are shown in Figure 2.5. Note the change in reflection response as a result of the different fracture geometries.
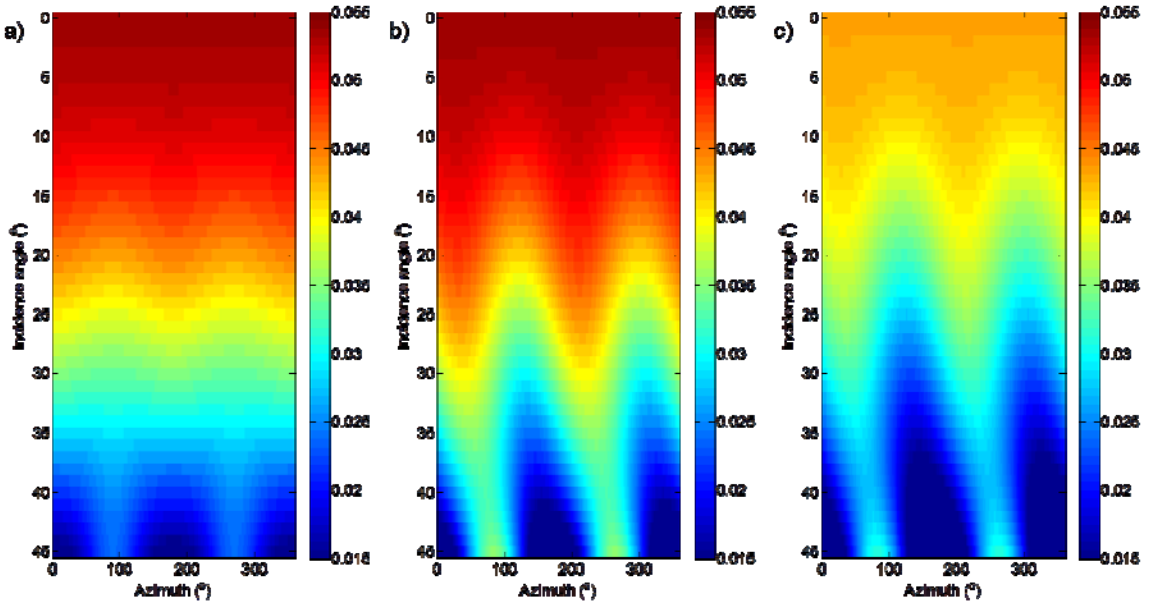
Figure 2.5. Reflection coefficients for a TI/TI model with a) vertical fractures in its natural coordinate system and the same symmetry axis azimuth above and below the reflecting interface, b) a 60 degree azimuthal rotation in the upper medium relative to the model in a) and c) a 60 degree azimuthal rotation in the upper medium and a 20 degree dip rotation in the lower medium relative to the model in a).

2.4 Inversion

In this section, we discuss the inversion procedure to estimate fracture parameters from reflection seismic data. The forward model can be formulated as

$$G(m) = d + e,\tag{2.14}$$

where G represents the forward operator, m represents the model parameters, d is the data and e is the error. The inverse problem is then the process from which a set of model parameters is estimated given an observed data set.

2.4.1 Forward model

In our formulation of the forward problem, we assume an Earth model consisting of TI layers, where the transverse isotropy is due to the presence of an aligned fracture system

24

as discussed above. Beginning with an isotropic background medium defined by the Lamé parameters, λ and μ and density, we use the linear slip deformation model of Schoenberg and Sayers (1995) to insert fractures through the addition of a normal (Z_N) and tangential (Z_T) fracture compliance (Appendix A). Subsequently, the inverse is calculated to obtain the effective elastic stiffness matrix for a medium containing fractures. In addition, a coordinate rotation about the x_3 axis is performed to represent the fracture azimuth. Fracture dips are not considered in the present inversion. The parameterization of the problem is therefore in terms of λ, μ, density, normal and tangential fracture compliance and fracture azimuth. Once the effective elastic stiffness parameters are calculated for each layer, equation 2.12 is used to generate the reflectivity response as a function of incidence angle and measurement azimuth. Subsequently, a convolution with a wavelet is performed to generate a set of synthetic azimuthal angle gathers. The input data required for the inversion are then normal moveout (NMO) corrected gathers where wave propagation effects have been addressed in separate processing and imaging steps. The forward modeling flowchart is illustrated in Figure 2.6.
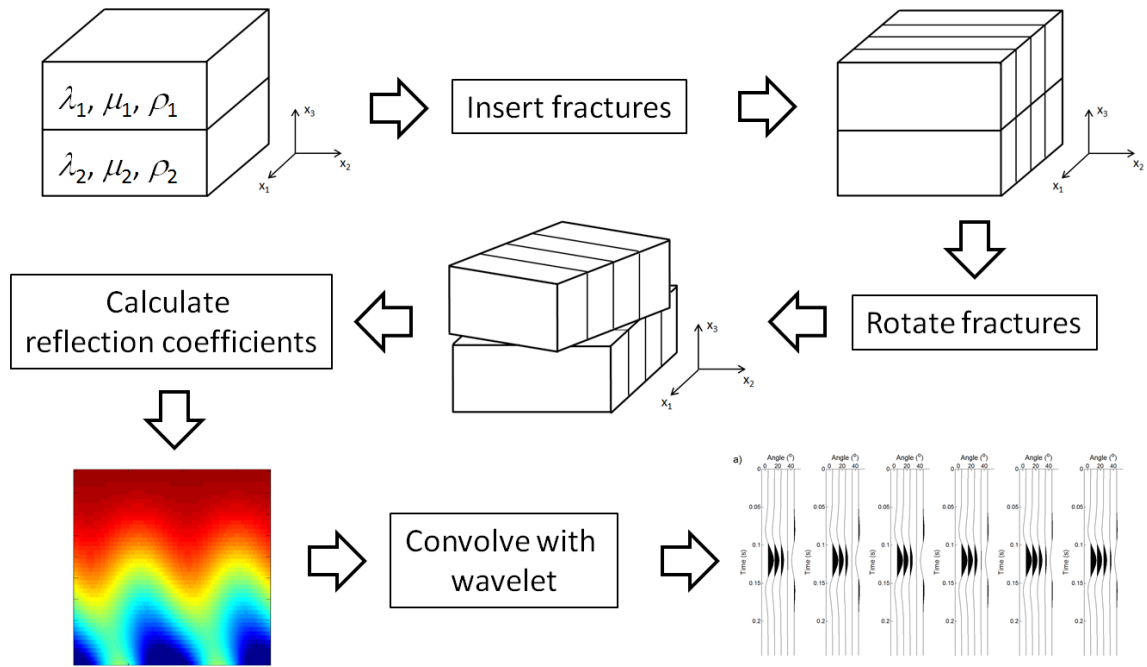
Figure 2.6. Forward modeling flowchart for synthetic data generation. The text boxes indicate the steps contained in the forward operator, G, in equation 2.14.

2.4.2 Simulated annealing

The forward modeling procedure as discussed above is non-linear. Therefore an iterative scheme is required to perform the inversion where an initial model is updated iteratively to obtain an optimal solution. Here, we use the simulated annealing algorithm, which belongs to the class of global optimization schemes capable of locating the global minimum of a given function. This optimization scheme mimics a physical process in which a solid in contact with a heat bath is slowly cooled until it reaches a state of minimum internal energy. The original Metropolis algorithm (Metropolis et al., 1953) that describes the simulated annealing process involves a random walk in the model or solution space. At each step, an error energy, E, which is defined by an objective function is calculated for the randomly selected solution. The acceptance criterion for that solution

26

is then defined by a change in energy, $\Delta E < 0$. However, if $\Delta E > 0$, a new solution is accepted with a probability exp($-\Delta E/T$), where T is the temperature of the system. T is slowly lowered throughout the execution of the algorithm and the system eventually reaches a state of equilibrium or the final solution. The optimal solution is therefore achieved through the minimization of the objective function. However, convergence is only guaranteed for a high initial temperature and very slow cooling, which requires enormous compute times. Therefore, the annealing schedule, which is the rate at which the temperature is lowered, becomes a crucial aspect of the inversion process.

Here, we use an alternative implementation of the algorithm as presented by Rothman (1986) for a residual statics problem and implemented by Sen and Stoffa (1991) for a 1D full waveform inversion. As opposed to the original algorithm which computes a solution prior to acceptance, the probability of acceptance is computed prior to the selection of a solution for a faster implementation. For a given model parameter, the energy is computed for every value in a discretized interval representing the allowable search range while keeping all other parameters constant. Subsequently, the probability distribution associated with the canonical ensemble as given by the Boltzmann distribution is calculated using

$$P(m_{ij}) = \frac{\exp\left(-E(m_{ij})/T\right)}{\sum_{j}\exp\left(-E(m_{ij})/T\right)},$$

(2.15)

where the subscript i represents the model parameters and the subscript j represents the range of values the model parameter, m_i can take. In equation 2.15, Boltzmann's constant, which is the physical constant relating the energy and the temperature, has been

absorbed into the temperature variable. A sample is then drawn from the distribution and retained as the new solution for m_i. This procedure is repeated for all model parameters and represents one iteration. The algorithm then takes the system through subsequent iterations where T is lowered according to a defined annealing schedule.

In this study, we use a two term objective function defined by

$$E = \sum (G(m)-d)^2 + \sum_k w_k \sum (1-m/m^{(initial)})^2 , \qquad (2.16)$$

where w_k is a weight applied to the kth elastic property and $m^{(initial)}$ represents the initial model used. The first term represents an L_2 norm of the data residuals and the second term controls the deviation from the initial model. Since the initial model is typically obtained through an averaging of measured well log values, it is assumed that the solution is close to the initial model. Therefore, the second term represents a perturbation and penalizes models based on their distance from the initial model.

2.4.3 Synthetic results

The data used in the inversion were generated using the forward model as discussed in §2.4.1. A two layered Earth model was created where the top layer is isotropic and the bottom layer has a set of vertical fractures. The model parameters are listed in Table 2.1.

Table 2.1. Model parameters for the two layered Earth model.

	λ (GPa)	μ (GPa)	ρ (kg/m^3)	Z_N (GPa^{-1})	Z_T (GPa^{-1})	ϕ (°)
Layer 1	5.29	6.80	2100	0	0	0
Layer 2	4.93	8.80	2200	0.01	0.01	40

For the inversion parameters, an initial temperature, T_0 was chosen to be 0.05 with an annealing schedule defined by $T_n=T_0*0.6^n$, where n represents the iteration number. The

inversion was performed using 20 iterations. Figure 2.7 shows histograms representing the Boltzmann distribution for the model parameters of the top layer after 5, 10 and 15 iterations. Note the width of the distribution narrows as the temperature decreases with each iteration, converging to a final solution. However, the rate at which the distributions narrow are different for the various model parameters. For the current parameterization, λ, μ and density converge at a much faster rate than the normal and tangential fracture compliances and fracture azimuth. The histograms therefore provide a representation of the sensitivity of each model parameter to the annealing schedule, and can be used to understand the convergence properties of the inversion. For example, if *a priori* information exists that places a constraint on certain parameters, additional search efforts in the solution space can be made for other parameters to ensure proper convergence to an optimal solution.

Figure 2.8 shows the data, synthetic data and residuals associated with the inversion. An excellent match between the data and synthetic data is observed, suggesting the inversion algorithm performed the intended task of minimizing the data residuals. Figure 2.9 shows the inversion results along with the true model and initial model. The results demonstrate a reasonable estimate of the model parameters with variable errors. Since the data residuals are small as shown in Figure 2.8c, the errors are attributed to the parameterization of the problem where the sensitivity to the objective function is variable for each model parameter. Also note the estimated fracture azimuth does not contain a 90° ambiguity. Although the overburden is isotropic, the inversion treats all layers as transversely isotropic and correctly estimates the fracture parameters.
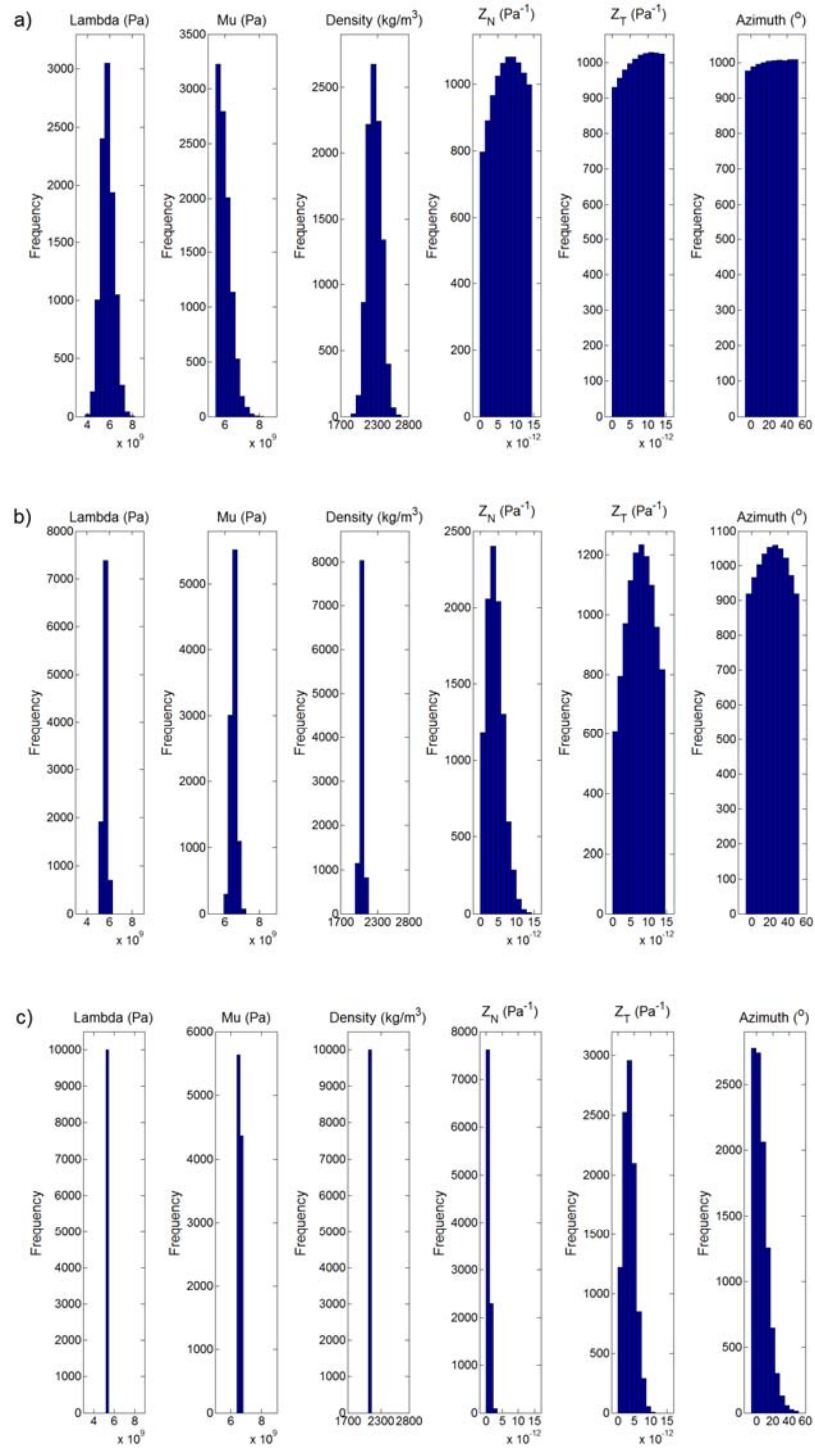
Figure 2.7. Histograms representing the Boltzmann distribution for the model parameters of the top layer after a) 5, b) 10 and c) 15 iterations.
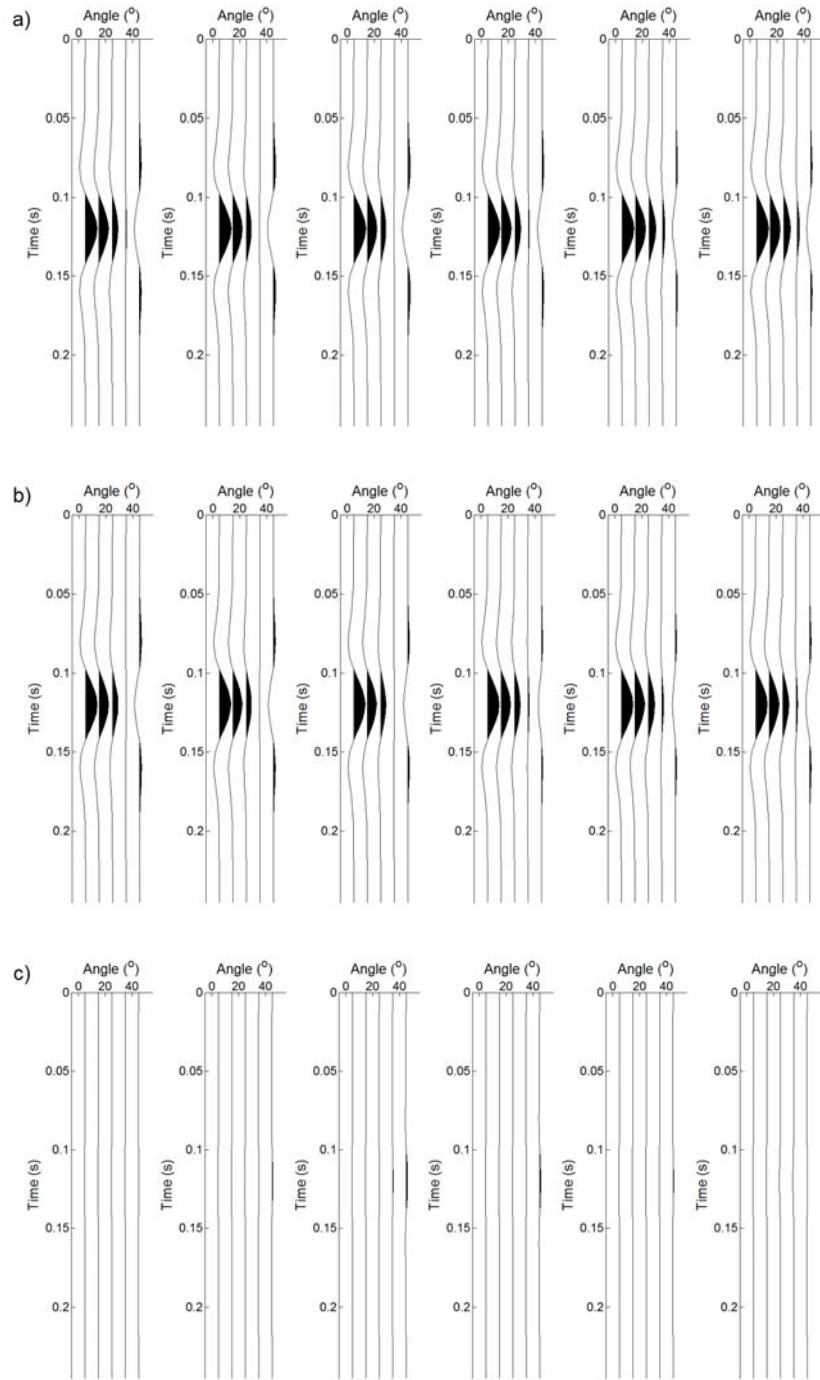
Figure 2.8. Azimuthal angle gathers representing the a) data, b) synthetic data and c) residuals associated with the inversion. Each panel represents a single azimuth of 30, 60, 90, 120 and 150 degrees from left to right for incident angles of 5, 15, 25, 35 and 45 degrees.
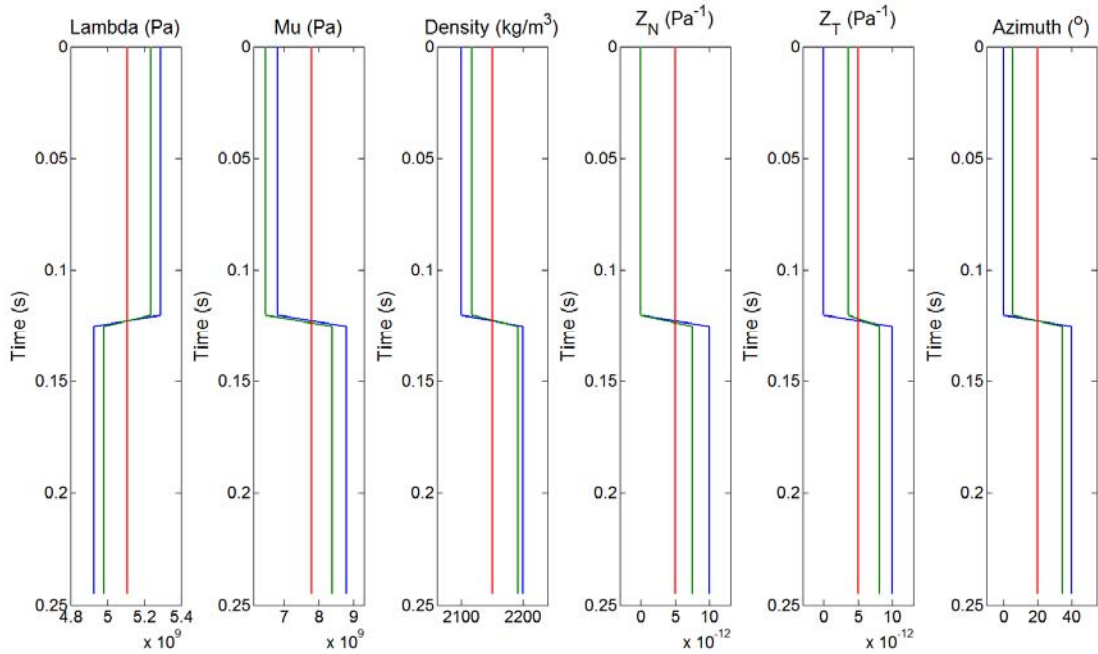
Figure 2.9. Results of the inversion illustrating the true model (blue), initial model (red) and inverted model (green).

2.5 Chapter summary

Arbitrary fracture orientations require a treatment of the TI reflection problem that includes coordinate transformations to represent the specific fracture geometries. In addition, due to the increased complexity of the rotated elastic stiffness matrix, a formulation of the reflection coefficient for arbitrary anisotropy is required to provide a more accurate description of P-wave reflections from fractured media.

The synthetic results for a two layered Earth model demonstrate a reasonable estimate of the model parameters with an excellent match between the data and synthetic data. The associated errors are then attributed to the parameterization of the problem where the sensitivity to the objective function is variable for each model parameter.

The azimuthal AVO inversion presented here addresses several issues regarding conventional AVAZ techniques for fracture characterization. These include the estimation of layer properties rather than interface properties, a relaxed constraint on fracture orientations above and below the reflecting interface and a unique estimation of the symmetry axis azimuth. The proposed methodology provides a more general description of fractured media and allows for an improved estimate of fracture parameters.

Chapter Three

Isotropic methods for fracture inference

3.1 Introduction

Direct methods for fracture detection are typically performed through analysis of the azimuthal variations in the seismic response. However, data requirements for azimuthal analysis are often not fulfilled for many conventional seismic survey designs, and therefore inhibit its use for azimuthal techniques as discussed in chapter two. Alternative methods for fracture detection are then required given the data limitations.

In this chapter, we investigate the use of subsurface properties estimated from seismic analysis under isotropic assumptions to delineate fracture systems through a case study in the Second White Speckled Shale (SWS) of Alberta, Canada. The SWS is an organic rich Upper Cretaceous marine mudstone deposited throughout the Alberta basin. It is believed to be a regionally continuous hydrocarbon system serving as both a source and reservoir rock (Fraser and Catuneanu, 2004). The SWS is highly impermeable in its original state, therefore production is attributed to natural fractures that create sufficient volume for storage and permeable pathways for fluid flow. Exploration risk in the SWS is therefore reduced by the detection of fractured zones within the formation.

For the inference of the associated fracture systems, a multi-property analysis was conducted for a 3D seismic survey in the study area. Due to insufficient azimuthal sampling associated with the acquisition geometry, we are limited to an isotropic

analysis. However, by invoking anisotropic models to represent the fractured shale, we can investigate the corresponding effect of anisotropic media subjected to an isotropic treatment. Properties examined to infer the presence of fractures include structural attributes extracted from the final post-stack seismic image and elastic properties derived from pre-stack seismic measurements.

In the next section, we introduce *a priori* information that constrains the fracture orientations through consideration of the tectonic setting and available field evidence. Then we present the methodology for fracture detection and analyze the corresponding results to help reduce uncertainty for exploration in the SWS. For subsequent discussions, we follow the nomenclature of Lacazette (2000, 2009) where the term fracture is used to describe a general zone of mechanical failure and the terms fault and joint represent shear and extensional fractures respectively.

3.2 Inference from tectonic setting and field evidence for fracture orientations

3.2.1 Tectonic setting and fracture orientations

Fracture orientations are dictated by the stress regime under which they were formed, where shear fractures form at an acute angle to the direction of maximum principal stress and extensional fractures form perpendicular to the direction of minimum principal stress. This is illustrated by the block diagram in Figure 3.1. Hence, knowledge of the principal stress directions can be used to constrain fracture orientations.
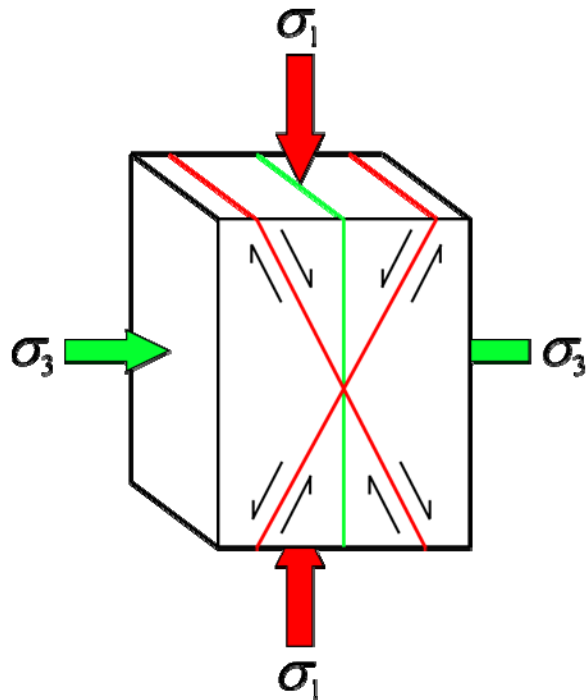
Figure 3.1. Block diagram illustrating the orientation of the maximum (σ_1) and minimum (σ_3) principal stresses and the corresponding fault (red) and joint (green) geometries.

The SWS formation accumulated during the Cenomanian-Turonian transgression of the Western Interior Seaway (Fraser and Catuneanu, 2004) approximately 90-100 Ma ago. This occurred during the formation of the North American Cordillera as a result of the Columbian orogeny from the mid-Jurassic to mid-Cretaceous and subsequently, the Laramide orogeny from the late-Cretaceous to Eocene. Due to their overlapping temporal and geographical boundaries, the two orogenies can be considered an orogenic continuum as advocated by Gabrielse and Yorath (1991). Therefore, we assume a single accretionary event, the Cordilleran orogeny, which supplies the horizontal compressive forces that were applied to the basin. The SWS is therefore subjected to contractional tectonics that contribute to fracture development. Figure 3.2 shows a map of the Canadian cordillera, where the direction of basin compression is oriented perpendicular to the eastern limit of

the Cordilleran deformation front and is oriented approximately NE-SW in the study area.
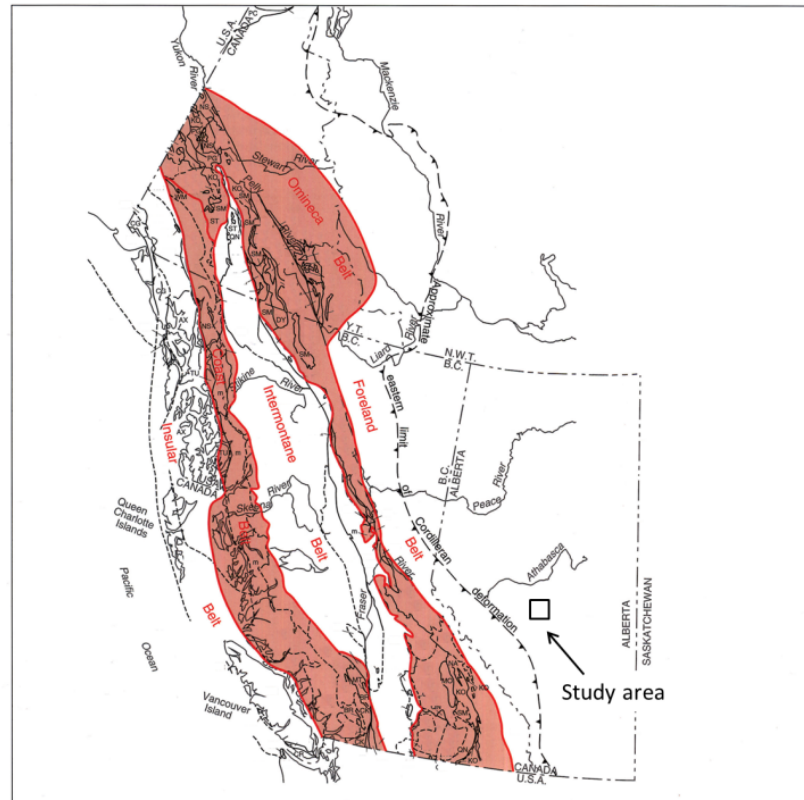
Figure 3.2. Map of the Canadian Cordillera with the location of the study area as indicated. Compression of the basin is oriented perpendicular to the eastern limit of the Cordilleran deformation front (Modified from Gabrielse and Yorath, 1991).

Figure 3.3 shows a NE-SW seismic section that was flattened on the base of reservoir horizon. At the SWS level, no seismically visible faulting is present. However, a subtle fold is apparent in the seismic data and folds are commonly associated with fractures.
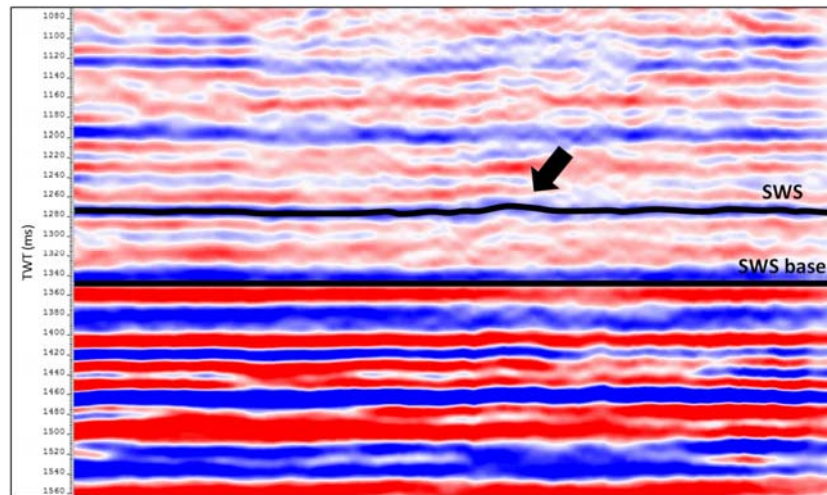
Figure 3.3. NE-SW seismic section that was flattened on the base of reservoir horizon. A subtle fold is evident in the seismic data.

Figure 3.4 shows a schematic diagram of a folded structure and the associated fracturing in its vicinity. As the lateral compressive forces associated with mountain building were oriented approximately NE-SW in the study area, the fold axis would strike NW-SE. If a fold is present, we can safely hypothesize a fracture set perpendicular to the fold axis and possibly another parallel to the fold axis with dips ranging from subvertical to subparallel to bedding. Furthermore, it is typical for joint sets to form in organic rich shales during oil and gas generation due to high in-situ fluid pressures (e.g., Engelder and Lacazette, 1990; Lacazette and Engelder, 1992). Therefore, a joint set is expected that is oriented perpendicular to the minimum principal stress direction that prevailed during the time of formation. In the following section, we provide evidence for the expected fracture orientations as discussed.
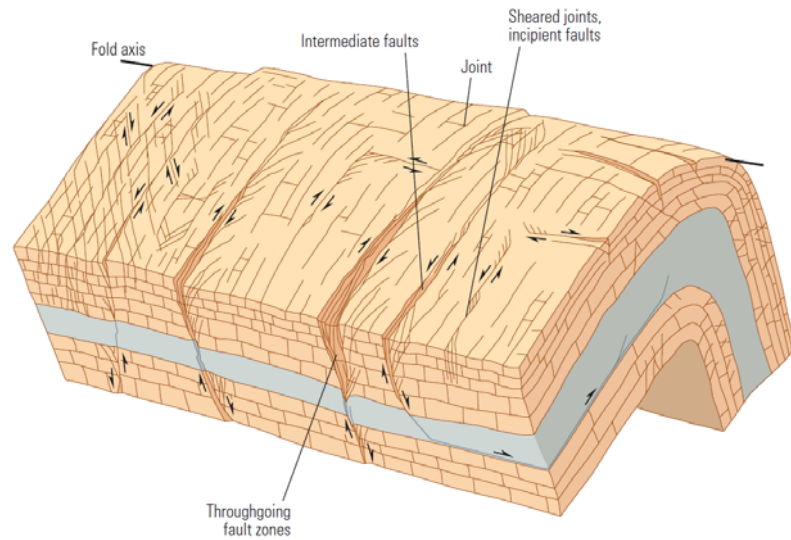
Figure 3.4. Schematic of a folded structure and the associated fracturing in its vicinity, where fractures form parallel and perpendicular to the fold axis (From Aarre et al., 2012, adapted from Florez-Niño el al., 2005).

3.2.2 Field evidence for fracture orientations

Here, we analyse production data from a nearby SWS reservoir outside the seismic survey. Using data from the wells highlighted in green as shown by the map in Figure 3.5a, a material balance (e.g., Lee et al., 2003) was performed to determine the expected pressure decline as the reservoir is depleted over time. The cumulative production for the wells is shown in the top of Figure 3.5b and is used to derive the reservoir pressure as shown by the black curve in the bottom of Figure 3.5b. In addition, the reservoir pressure measured independently at each well is plotted as points in the bottom of Figure 3.5b. Note the agreement between the pressure responses obtained from the two different sources. In conjunction with the geometry of the well positions, this suggests that the wells are in pressure communication, where this is possible only through the existence of permeable pathways or fractures that are oriented NW-SE, connecting the various wells.
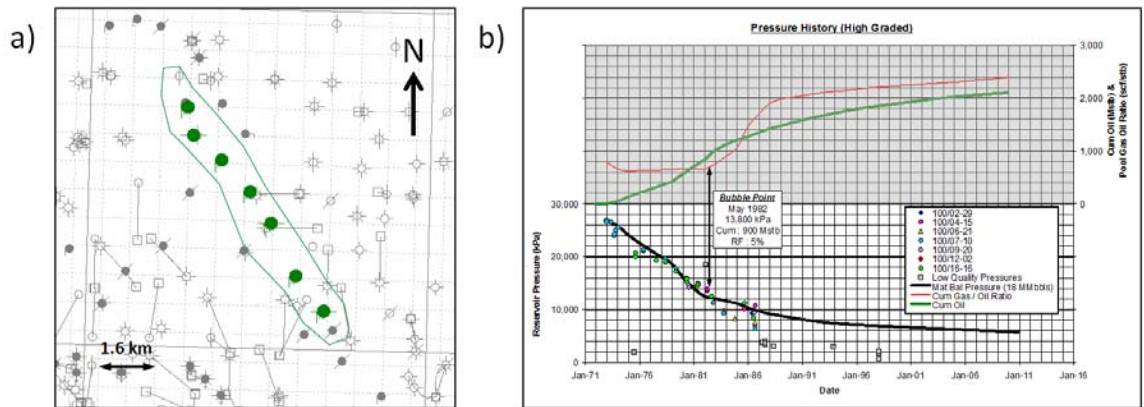
Figure 3.5. a) Map illustrating the locations of wells used for material balance and the corresponding b) cumulative production (top) and reservoir pressure (bottom) as a function of time. The reservoir pressure derived from material balance (black curve) is in agreement with those measured independently at each well (colored points), indicating pressure communication between the wells and the existence of permeable pathways or fractures oriented approximately NW-SE.

As discussed, the seismic survey in the study area was not adequately sampled for azimuthal analysis. However, we can increase the common mid-point (CMP) bin size to achieve a more complete sampling of the wavefield azimuthal variations, although at the expense of loss of spatial resolution. Figure 3.6 shows the resulting azimuthal offset gather corrected for NMO using an estimate of the vertical P-wave velocity, with a CMP location centered at a producing well within the seismic survey. In Figure 3.6, each panel represents a single azimuth ranging from 5° to 175° measured clockwise from north. In addition, the reflection event corresponding to the base of reservoir is outlined in red. Azimuthal variation of the traveltime response associated with the base of reservoir reflection is clearly visible, where maximum and minimum curvatures are observed at approximately 45° and 135° from north respectively. This response is hypothesized to be the result of wave propagation through a shale containing a series of aligned fractures. In

40

the following paragraphs, we discuss a fractured shale model and attempt to reproduce

the traveltime response as observed in Figure 3.6.
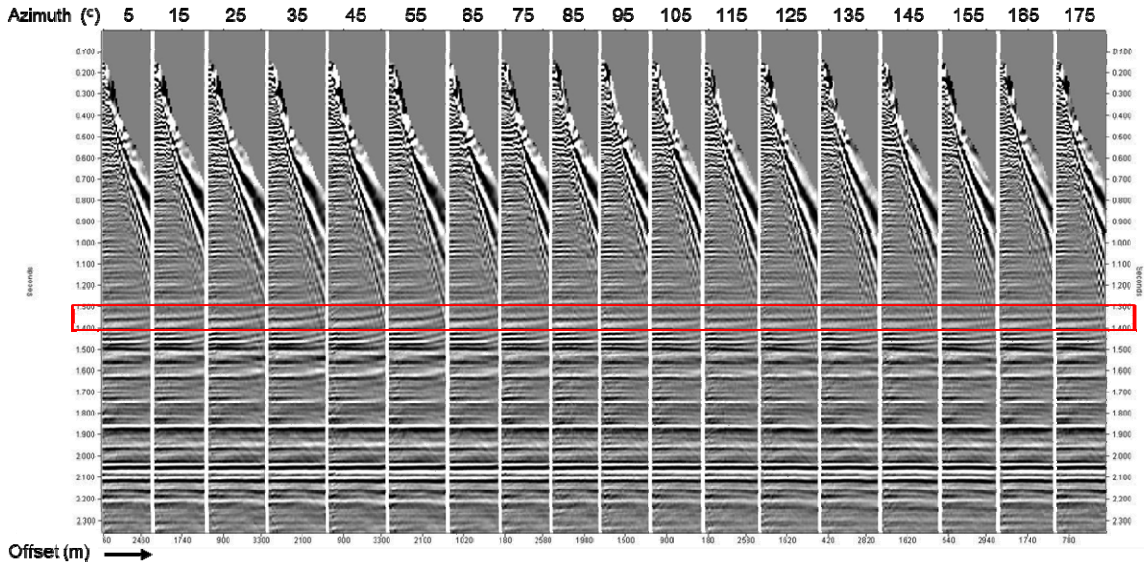
Figure 3.6. NMO corrected azimuthal offset gather for an area where fractures are known to exist. The azimuth ranges from 5° to 175° measured clockwise from north. Note the azimuthal and offset dependence of the traveltime response associated with the base of reservoir reflection outlined in red.

Most shales with low geological dip can be approximated as transversely isotropic

with a vertical axis of rotational symmetry (VTI) (Sayers, 2010), where the horizontal P-

wave velocity is faster than the vertical P-wave velocity. Therefore, we can use a VTI

medium to represent an unfractured shale and further simulate a set of aligned fractures

using Hudson's penny-shaped crack model (Appendix A). Figure 3.7 illustrates the

schematic of the fractured shale where a set of aligned cracks are inserted in the x_2-x_3

plane. Although multiple fracture sets are expected, the aligned vertical cracks represent

the most compliant set oriented perpendicular to the present day minimum horizontal

stress that would dominate the seismic response (e.g., Crampin, 1987). The resulting medium has an effective elastic stiffness tensor that exhibits an orthorhombic symmetry.
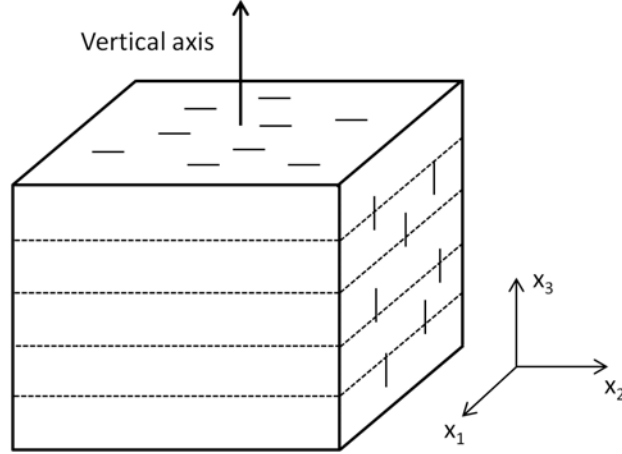
Figure 3.7. Schematic of a VTI medium with aligned fractures where the vertical axis coincides with the x_3 axis. The dashed lines and short solid lines represent the shale bedding and crack orientations respectively. The resulting medium has an elastic stiffness tensor that exhibits an orthorhombic symmetry.

In generating the traveltime response associated with seismic wave propagation through an orthorhombic medium, we use a linearized approximation for the quasi P-wave group velocity derived by Daley and Krebes (2006) given by

$$\frac{1}{V_{qP}^2(\bar{N})} \approx \frac{N_1^2}{A_{11}} + \frac{N_2^2}{A_{22}} + \frac{N_3^2}{A_{33}} - \frac{E_{12}N_1^2N_2^2}{A_{11}A_{22}} - \frac{E_{13}N_1^2N_3^2}{A_{11}A_{33}} - \frac{E_{23}N_2^2N_3^2}{A_{22}A_{33}}, \tag{3.1}$$

where

$$E_{12} = 2(A_{12} + 2A_{66}) - (A_{11} + A_{22}), \tag{3.2}$$

$$E_{13} = 2(A_{13} + 2A_{55}) - (A_{11} + A_{33}), \tag{3.3}$$

and

$$E_{23} = 2(A_{23} + 2A_{44}) - (A_{22} + A_{33}), \tag{3.4}$$

where A_{ij} represents the density normalized elastic stiffness parameters and $\bar{N}$ represents a unit vector along the direction of the raypath. The modeling was performed for a transmitted wave through the fractured zone that is subsequently reflected from the base of reservoir where traveltime anisotropy effects can be observed.
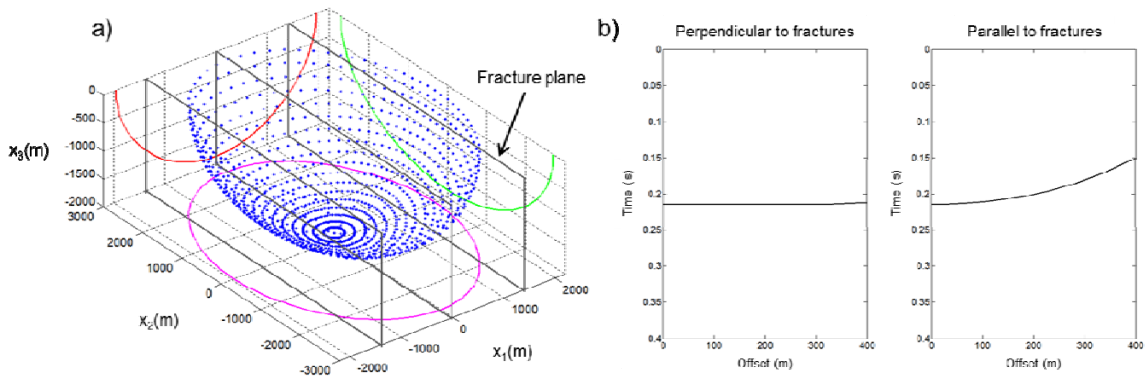
Figure 3.8. a) Wavefront through the fractured shale model at a snapshot in time and b) the NMO corrected traveltime curves for propagation directions perpendicular and parallel to the fractures.

The resulting wavefront through the fractured medium at a snapshot in time is illustrated in Figure 3.8a. Note the non-sphericity of the wavefront where the wave travels faster parallel to the fractures and slower perpendicular to the fractures. In addition, Figure 3.8b shows the NMO corrected traveltime curves for waves propagating in a direction perpendicular and parallel to the fracture plane, where the NMO correction was performed using the component of the elastic stiffness tensor that corresponds to the vertical P-wave velocity. For a propagation direction parallel to the fractures, the wave propagates as in an unfractured shale. The horizontal P-wave velocity parallel to fractures is greater than the vertical P-wave velocity, resulting in a reduced traveltime at increasing

offsets upon NMO removal. For a propagation direction perpendicular to the fractures, the horizontal P-wave velocity decreases due to the excess compliance of the fractures and this counteracts the effect of an increase in the horizontal P-wave velocity of the shale. This results in an NMO corrected traveltime that is not as greatly reduced relative to a propagation direction parallel to the fractures at increasing offsets. Therefore, according to the fractured shale model, the maximum and minimum traveltime curvature events for the base of reservoir reflection in Figure 3.6 correspond to wave propagation parallel and perpendicular to the fractures respectively. These results suggest that the azimuthal anisotropy observed in Figure 3.6 could be the result of fractures oriented at approximately N045°E. This is consistent with the expected orientation for open fractures in the present day stress regime where the minimum horizontal stress is oriented approximately NW-SE.

3.3 Fracture inference

Fractures that form in relation to mechanisms such as folding are likely to be accompanied by structural changes detectable at the seismic scale (e.g., Chopra and Marfurt, 2007). However, in an alternate scenario, fractures can also form as a result of conditions such as increased stresses due to burial, uplift and unloading, thermal contraction or high in-situ fluid pressures (e.g., Engelder and Lacazette, 1990; Lacazette and Engelder, 1992; Engelder and Fischer, 1996; English, 2012) that are common in unconventional reservoirs, which are self-sourcing and sealing. Consequently, faults and joints can form that are not directly correlated to seismic scale structural changes. In this

study, we consider the two scenarios separately and implement different methodologies for the inference of these fracture systems.

3.3.1 Fractures with structural controls

Fractures that are related to structural deformation such as folds can be detected as subtle changes in the seismic image (e.g., Chopra and Marfurt, 2007). Therefore, attributes that highlight structural changes in the post-stack seismic volume were used to identify areas that are likely to be fractured. Here, we use the ant tracking algorithm (Pedersen et al., 2002) to extract structural information from the seismic image. First, an edge-detection algorithm is applied to the post-stack seismic volume to detect all disruptions of reflector continuity that may correspond to changes in structure. Subsequently, the ant tracking algorithm uses swarm intelligence to extract features from within the edge-detection volume that exhibit consistencies in dip, azimuth, planarity, and spatial continuity. This provides an image that highlights areas with structural changes that are likely to correlate with fracturing. Figure 3.9 shows a map view of the ant tracking results extracted at the SWS level, which was computed with no directional bias. In addition, a time thickness map corresponding to the SWS was superimposed to illustrate the associated geometry of the structure. The map demonstrates a major structural feature represented by a collection of linear features in the ant tracking results and an anomalously thick zone trending NW-SE through the survey area. This is interpreted as a subtle fold where the main fold axis is indicated in the figure. Since the ant tracking algorithm illuminates planar features, the individual events correspond to either very subtle faults or local fold axial planes, where the associated fracturing in their vicinity can be inferred according to Figure 3.4.

However, fractures on the flanks are not directly imaged using this technique and consequently, the lateral extent of the associated fractures is ambiguous.
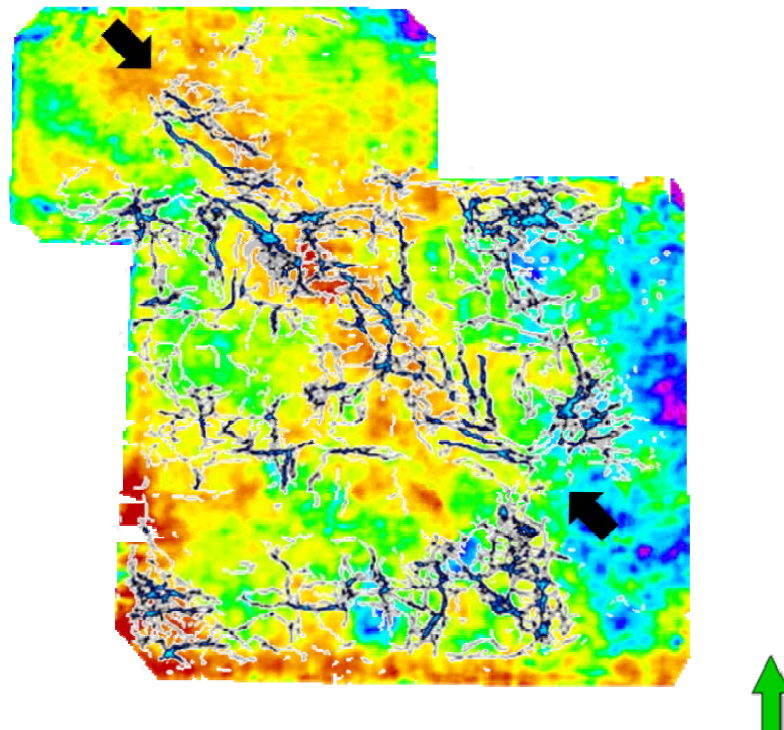
Figure 3.9. Map view of the ant tracking results superimposed on a time thickness map at the SWS level. Hot colors represent a thickening of the strata. The major structural feature trending NW-SE is interpreted as a subtle fold.

3.3.2 *Fractures without structural controls*

Fractures can also form under conditions that are not necessarily accompanied by seismic scale structural changes. Therefore, the detection of these fracture systems was achieved through an investigation into the elastic properties that control failure and to determine the elastic response of fractures. To determine the elastic properties, a pre-stack AVO inversion was performed to extract the P- and S-wave velocities and density. At the target

depth, P-wave incidence angles of up to 43° were available, providing sufficient angle coverage to confidently perform a three term AVO inversion. Subsequently, the constitutive relations were applied for the transformation to geomechanical properties (Poisson's ratio and Young's modulus) that are important in fracture mechanics.

3.3.2.1 Elastic properties and failure

In this section, we briefly discuss the relationship between elastic properties and material failure in order to determine the conditions that are most favorable for fracture formation. There is an extensive body of literature on this subject where various failure criteria can be used to describe the conditions under which a material will fail under stress, therefore we simply comment on a few results.

The Coulomb failure criterion (Coulomb, 1773) can be used to understand the conditions under which a material will fail in shear for the formation of a fault. It states that when the shear stress, τ, exceeds the cohesion, S_0, of a material, failure will occur. This criterion can be illustrated using a Mohr diagram as shown in Figure 10. In the context of the Mohr diagram, failure occurs when the Mohr circle, whose diameter is controlled by the difference between the maximum and minimum principal stresses, is tangent to the failure envelope (dashed circle in Figure 3.10). This is the condition such that the maximum and minimum principal stresses create a shear stress that exceeds the cohesion of the material.
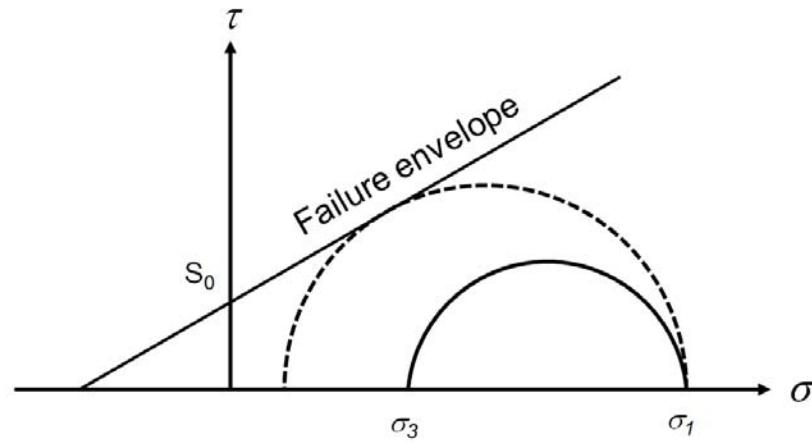
Figure 3.10. Mohr diagram representation of the Coulomb failure criterion. Shear failure occurs when the Mohr circle is tangent to the failure envelope (dashed circle) where the maximum (σ_1) and minimum (σ_3) principal stresses create a shear stress (τ) that exceeds the cohesion (S_0) of the material.

Now consider the uniaxial strain equation given by

$$\sigma_3 = \frac{v}{1-v}\sigma_1, \tag{3.5}$$

where v represents the Poisson's ratio while σ_1 and σ_3 represent the maximum and minimum principal stresses respectively. Equation 3.5 states that for a given value of the maximum principal stress, the minimum principal stress is only dependent on v. As v decreases, the value of the minimum principal stress also decreases, resulting in a larger Mohr circle. Therefore, a material with a lower Poisson's ratio is more easily fractured for a given load under the conditions of uniaxial strain.

In addition, the Griffith (1920) energy-balance criterion can be used for the description of joint propagation. It provides a relationship between the elastic properties of a material and the critical tensile stress required for crack growth, where a decrease in the Poisson's ratio and Young's modulus lowers the critical crack propagation stress (see

Jaeger et al., 2007, p. 309). However, these parameters are not independent but are linked by the material constitutive relations. Consider the relationship given by (e.g., Sheriff and Geldart, 1995)

$$E = 3K(1 - 2\nu),$$ (3.6)

where E is the Young's modulus and K is the bulk modulus. For a constant value of K, equation 3.6 is linear and a decrease in ν is necessarily accompanied by an increase in E. A decrease in E in association with a decrease in ν can then be achieved by lowering the value of K. Therefore, a material with a low Poisson's ratio and a relative low in the Young's modulus presents more favorable conditions for fractures to form.

3.3.2.2 Elastic properties of fractured media

Thus far, only an isotropic elastic medium has been considered. In addition, the static definition of the elastic moduli was used, which corresponds to those that would be directly measured in a deformational experiment. The specific definition used for Poisson's ratio is the negative ratio of two transverse strain components and the definition used for Young's modulus is the constant of proportionality between the stress and strain along a single dimension. Alternatively, the static moduli can be computed using the above definitions given knowledge of the complete elastic stiffness matrix. These definitions are important for understanding failure as discussed in the above section. Conversely, Poisson's ratio and Young's modulus can be computed using the wave propagation velocities, which are referred to as the dynamic moduli. These can be computed using specific components of the elastic stiffness matrix corresponding to the wave propagation velocities. Under isotropic conditions, the elastic moduli computed

using the static and dynamic definitions are equivalent due to symmetry relations of the isotropic elastic stiffness matrix. However, if anisotropy is introduced, the dynamic moduli deviate from the static definition. This is the result of a lower symmetry system associated with anisotropic media, and because the static and dynamic moduli are calculated differently, they provide different information about the medium. The wave propagation velocities are obtained from AVO inversion, therefore, we need to investigate the effect of fractures on the dynamic elastic moduli for a proper interpretation of the results. Note that the static and dynamic moduli as discussed are in the context of their mathematical forms rather than differences in their measured values due to different strain amplitudes between the static and dynamic experiments.

Since the most compliant fracture set is oriented perpendicular to the present day minimum horizontal stress and would dominate the seismic response (e.g., Crampin, 1987), we perform the modeling using a set of vertical aligned cracks. The corresponding dynamic Poisson's ratio has a fast and slow component due to shear wave birefringence (Crampin, 1987) and is given by

$$\nu_{fast} = \frac{V_P^2 - 2V_{S,fast}^2}{2\left(V_P^2 - V_{S,fast}^2\right)} = \frac{C_{33} - 2C_{44}}{2\left(C_{33} - C_{44}\right)},$$
(3.7)

and

$$\nu_{slow} = \frac{V_P^2 - 2V_{S,slow}^2}{2\left(V_P^2 - V_{S,slow}^2\right)} = \frac{C_{33} - 2C_{55}}{2\left(C_{33} - C_{55}\right)},$$
(3.8)

where V_P and V_S represent the P- and S-wave velocities respectively and C_{ij} represents the effective elastic stiffness parameters. In equations 3.7 and 3.8, C_{33}, C_{44}, and C_{55} correspond to the vertical P-wave velocity and the two orthogonal polarizations of the

50

fast and slow vertical S-wave velocity respectively. Likewise, the dynamic Young's modulus has a fast and slow component and is given by

$$E_{fast} = 2C_{44}\left(1 + v_{fast}\right),$$ (3.9)

and

$$E_{slow} = 2C_{55}\left(1 + v_{slow}\right).$$ (3.10)

The difference between the static and dynamic moduli, once anisotropy is introduced, results from an increase in the number of independent elastic stiffness parameters. For comparison, the various components of the static Poisson's ratio and Young's modulus for an orthorhombic medium as expressed in terms of the elastic stiffness parameters are given in Appendix B. The static moduli are functions of only C_{11}, C_{22}, C_{33}, C_{12}, C_{13}, and C_{23} and are therefore independent of the S-wave propagation velocities. The dynamic moduli as computed using equations 3.7 to 3.10 include the S-wave velocities and therefore deviate from the static definition and must be interpreted differently.
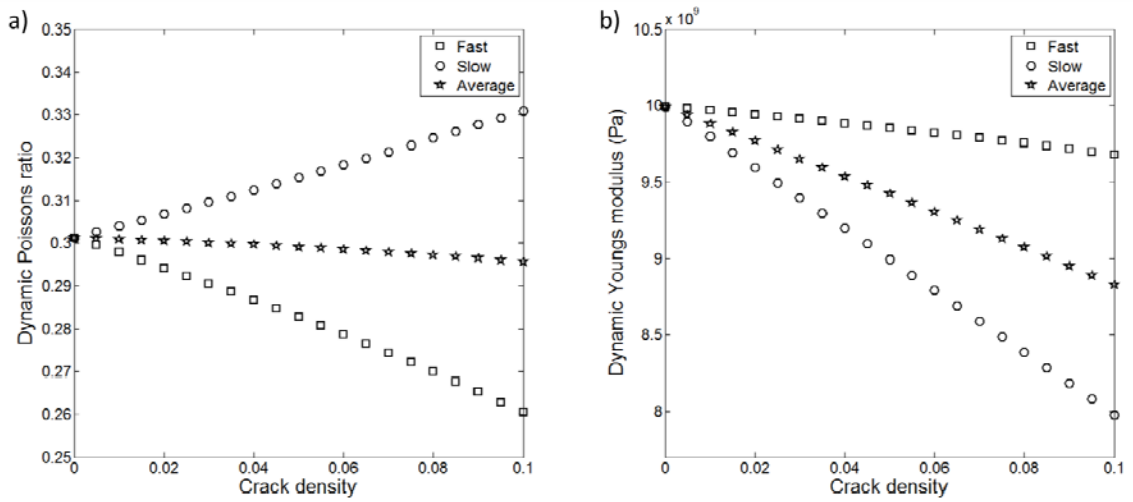
Figure 3.11. a) Dynamic Poisson's ratio and b) Young's modulus as a function of crack density calculated using equations 3.7 to 3.10 and A-1, A-4, A-5 and A-6.

Figure 3.11 shows the fast, slow, and average values of the dynamic Poisson's ratio and Young's modulus as a function of crack density calculated using equations 3.7 to 3.10 and A-1, A-4, A-5 and A-6. For the isotropic analysis performed here, the fast and slow directions are not considered independently. Therefore, the estimated elastic properties are approximated as an average of the extrema. The fast component of the dynamic Poisson's ratio is a decreasing function of crack density, where the P-wave velocity decreases while the S-wave velocity parallel to the fractures is unchanged with increasing crack density (Appendix A). The slow component of the dynamic Poisson's ratio is an increasing function of crack density, where the P-wave velocity and S-wave velocity perpendicular to the fractures both decrease with crack density. However, the S-wave velocity decreases at a greater rate relative to the P-wave velocity, resulting in an increase in the Poisson's ratio with an increase in crack density (Appendix A). Therefore, the response of the average dynamic Poisson's ratio is largely unchanged for increasing

crack density (Figure 3.11a). This suggests that an increase in fracturing has a minimal effect on the average dynamic Poisson's ratio. Therefore, we identify low values of the dynamic Poisson's ratio as more favorable conditions for the formation of fractures in a given stress environment rather than a direct indicator for the presence of fractures. Conversely, the fast, slow and average dynamic Young's modulus all decrease with an increase in fracturing (Figure 3.11b). Therefore, we identify low values as an indicator for the presence of fractures.

The vertical P-wave velocity can also be used as an indicator for the presence of fractures. Again, using Hudson's penny-shaped crack model, we can investigate the vertical P-wave response of a fractured medium. According to Hudson (1981), the first order perturbation of C_{33} contains the crack density term and is always negative (Appendix A). Therefore, an increase in crack density results in a decrease in the effective vertical P-wave velocity. Using this result, we identify anomalous zones with a decrease in the vertical P-wave velocity as an indicator for the presence of fractures.

Given the above analysis, three properties are used to infer the presence of fracture systems not directly correlated to seismic scale structural changes. These include the dynamic Poisson's ratio and Young's modulus and vertical P-wave velocity. As discussed above, low values are desired for all properties. Figures 3.12a to 3.12c show horizon slices for the various properties extracted at the SWS level.
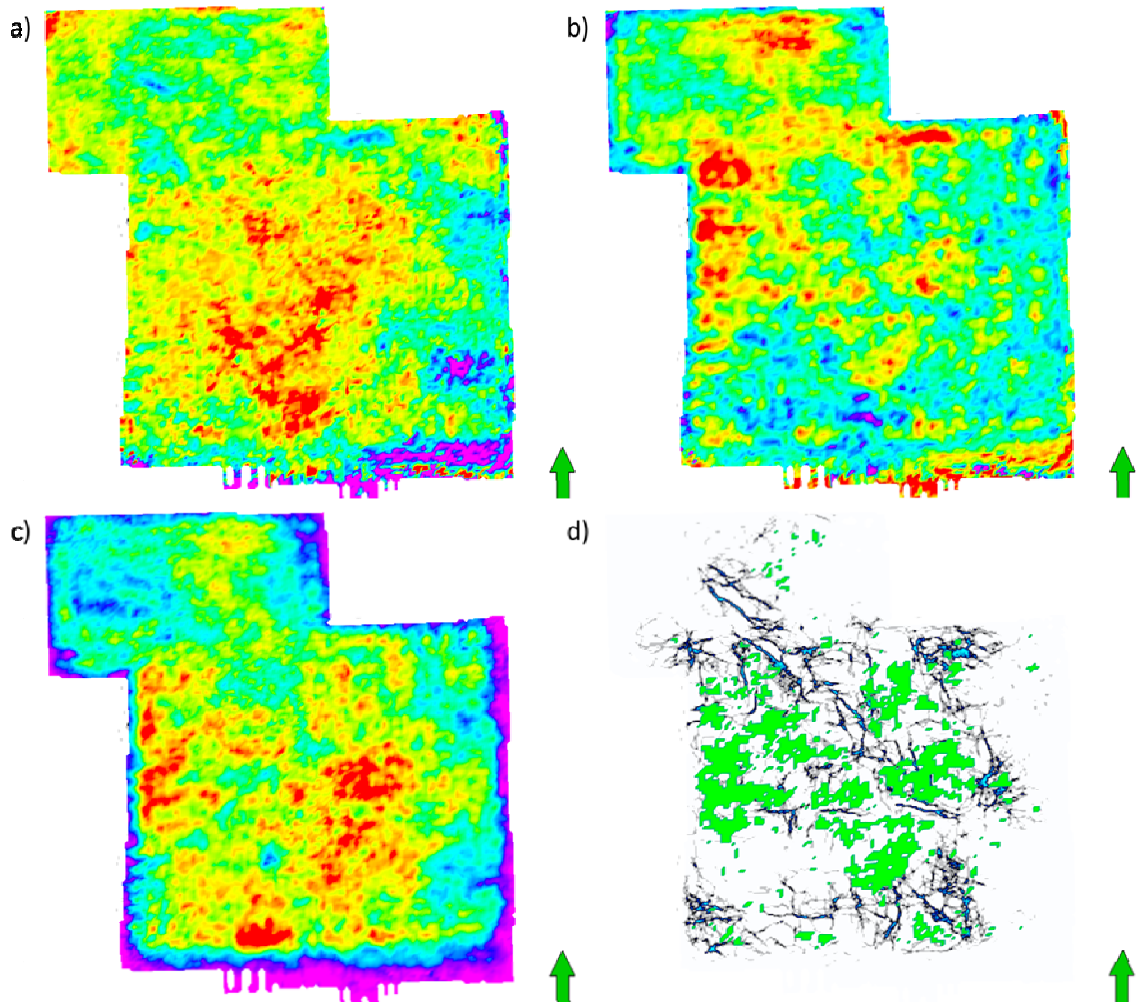
Figure 3.12. Horizon slice of the a) dynamic Poisson's ratio, b) dynamic Young's modulus and c) P-wave velocity extracted at the SWS level where hot colors represent low values for the three properties. These are combined with the ant tracking results to create the d) multi-property map illustrating areas that are likely to be fractured.

3.3.3 Multi-property analysis

To infer the presence of fractures in the SWS, we implement a multi-property analysis to identify areas that are most likely to be fractured based on structural information and elastic properties of the medium. The above analysis provides possible responses related to fractures. However, the responses could be the result of phenomena not yet considered

such as laterally changing lithology. Therefore, to reduce uncertainty associated with each individual property, we combine all the information acquired from the above analysis to increase our confidence.

Figure 3.12d shows the results of the multi-property analysis. The green areas combine information from the three elastic properties, indicating the possible locations of fractures not directly correlated to seismic scale structural changes. To identify these areas, threshold values were defined for each elastic property and areas that fell within the accepted range for all three properties were flagged as potential locations for the presence of fractures. In addition, the ant tracking results were overlaid for the identification of areas with seismic scale structural changes from which the associated fracturing can be inferred. The map demonstrates that the green areas are mostly concentrated adjacent to the structure trending NW-SE, corresponding to the flanks of the interpreted fold. Furthermore, there exists a gap along the main structural feature where the elastic properties do not fit the criteria for the presence of fractures. This is consistent with a contractional fault-bend fold (e.g., Suppe, 1983; Salvini and Storti, 2001), where an undeformed zone exists at the crest of the fold that should not be fractured as illustrated in Figure 3.13. From the ant tracking image alone, the lateral extent of the fold related fractures are ambiguous, however, with the additional analysis that includes the elastic properties, the lateral extent of these fractures can be inferred.
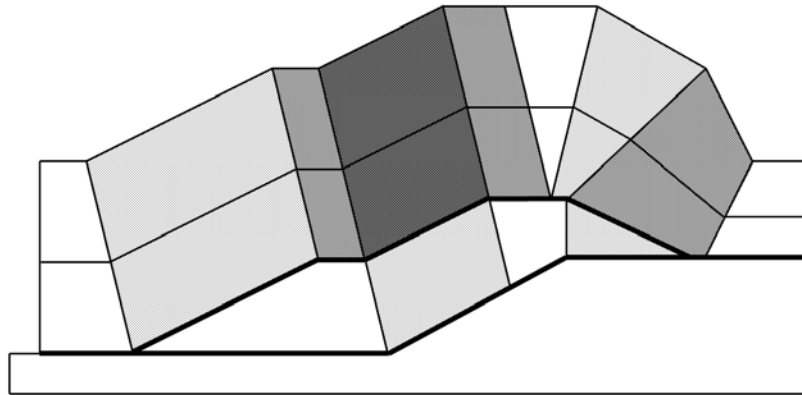
Figure 3.13. Schematic of a contractional fault-bend fold where the shading is representative of the fracture intensity. An undeformed zone exists at the crest of the fold that should not be fractured (Adapted from Salvini and Storti, 2001).

3.4 Chapter summary

The presence of fractures in the SWS was inferred through a multi-property analysis which includes structural attributes extracted from the seismic image and elastic properties estimated through AVO inversion. The structural attributes identified areas with seismic scale structural changes from which the associated fracturing in the vicinity of these features can be inferred. The elastic property estimates identified areas with an increased likelihood of fractures not directly correlated to seismic scale structural changes. In the study area, a subtle fold was identified through the ant tracking results. Furthermore, investigation into the elastic properties of fractured media revealed locations on the flanks of the fold that are likely to be fractured, which identified the lateral extent of these features that was not possible from structural attributes alone as discussed in §1.1.2. The combined interpretation of these results suggests the existence of a contractional fault-bend fold, where an undeformed zone exists at the crest of the fold that should not be fractured as indicated by the multi-property map.

56

In situations where the available seismic data is not adequate for unambiguous azimuthal analysis, alternative methods for fracture detection become necessary. Information concerning fractures can be extracted from conventional isotropic seismic analysis techniques and used to reduce uncertainty for the delineation of the associated fracture systems.

Chapter Four

Hydraulic fracture response of pre-rupture faults

4.1 Introduction

Hydraulic fracture stimulation plays a vital role in the development of unconventional energy resources, where the objective is to create permeable pathways for fluid flow. Issues that often arise are associated with variations in the in-situ stress field over relatively small distances, where deviations from the regional stress field are observed. Areas that are often prone to these variations are in the vicinity of faults or structural features related to tectonic loading, where mechanical alterations in the rock mass result in changes to the material properties and its associated stress response, and upon stimulation, unexpected fracture patterns can result.

The mechanisms responsible for hydraulic fracturing are numerous and many are beyond the capacity of existing theories. However, simple models can be constructed to aid in the understanding of the complex phenomenon. In this chapter, we present a model to explain the complex fracture behavior observed in the stimulation program associated with an unconventional gas well in the Montney shale of NE British Columbia, Canada. This study stems from the work of Norton et al. (2010) and Maxwell et al. (2011), where a reservoir characterization study was performed through analysis of surface seismic data and the associated microseismicity recorded during stimulation. We being with an

overview of the work done previously and proceed with the presentation of a micromechanical model that seeks to explain the observed fracture behavior.

4.2 Background

The Montney is a Lower Triassic succession of organic rich siltstones and shales deposited in a shallow-water shoreface to deep-water marine setting. Gas is trapped as a continuous phase in the fine grained, low permeability sediments where capillary forces restrict migration up-dip or into overlying coarser grained rock. This results in a self-sourcing and sealing hydrocarbon system that is generally overpressured. The target interval is at approximately 1750 m TVD with porosities ranging from 0.03 to 0.06 and permeabilities ranging from 0.001 to 0.05 mD. These characteristics result in an unconventional reservoir where hydraulic fracturing is necessary to achieve economic recovery rates.

The work of Norton et al. (2010) and Maxwell et al. (2011) combined properties derived from reflection seismic data and microseismic measurements to characterize the variations in reservoir properties and the stimulation response. Figure 4.1 shows the variability in the microseismicity associated with the stimulation program of three horizontal wells. The microseismicity shown correspond to events above a magnitude cut-off that removes any detection bias within a distance of 1000 m from the monitoring well (Maxwell et al., 2011).
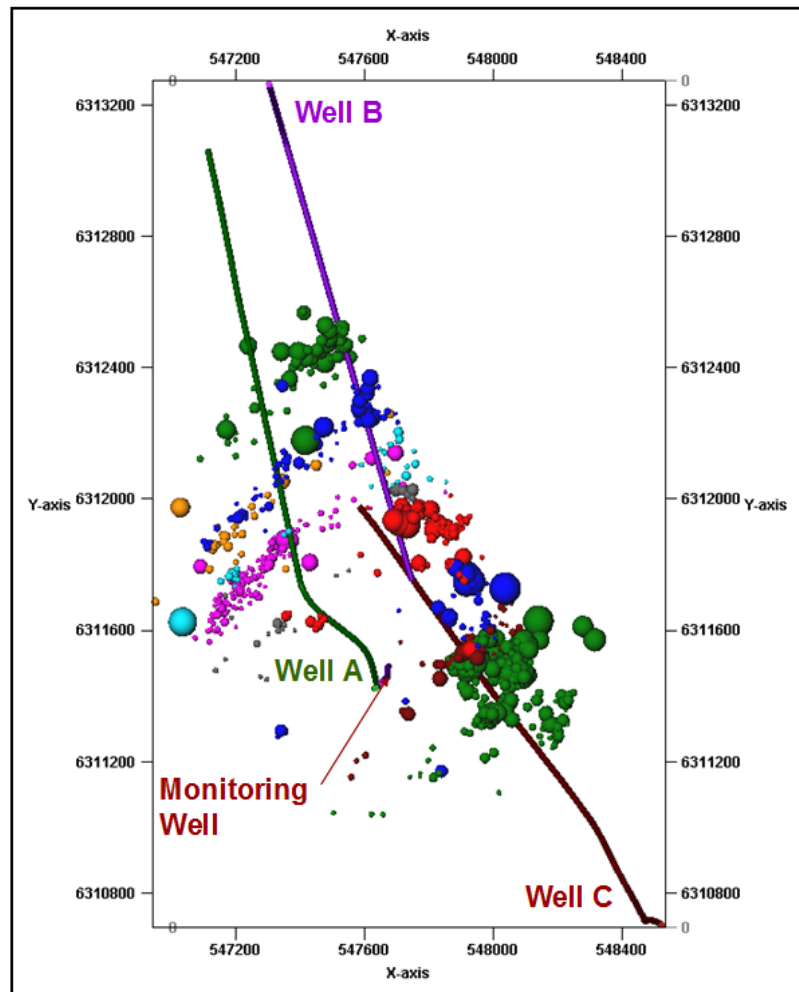
Figure 4.1. Map view (north is up) illustrating the variability in the microseismic response associated with the stimulation of three horizontal wells. The wells were drilled approximately parallel to the regional minimum principal stress direction. The color and size of the spheres represent the various stages of the hydraulic fracture treatment and the magnitude of the microseismic events respectively (From Maxwell et al., 2011).

In addition, only stages nearest to the monitoring well were taken into account (10 out of 21 stages). This was performed to ensure the presence of sufficiently high signal to noise levels for subsequent data analysis. In Figure 4.1, large variations in the microseismic response are clearly seen where events SW of Well A exhibit a NE-SW trend that

60

propagate away from the wellbore while events along the length of Wells B and C are constrained to a linear region trending NW-SE.

To investigate these variations, Maxwell et al. (2011) performed additional analysis on the induced microseismicity to determine the nature of deformation associated with the hydraulic fracture treatment. Figure 4.2 shows calculations of the seismic moment density and b-values associated with the event clusters to investigate the microseismic source strength (Maxwell et al., 2006) and frequency-magnitude relationship (Gutenberg and Richter, 1954) respectively. The moment densities SW of Well A are relatively small while the moment densities along Wells B and C are larger, where the increased source strength is consistent with fault activation along Wells B and C. Additionally, b-values can be used to distinguish between fault activation and hydraulic fractures, where fault activation results in b-values of approximately one while higher values are associated with hydraulic fractures (e.g., Maxwell et al., 2009). Low b-values of around one are observed along Wells B and C, indicating the microseismicity in this region is associated with fault activation, and is consistent with the conclusions made from observations of the larger moment densities. Conversely, higher b-values are observed SW of Well A and are consistent with conventional hydraulic fractures.
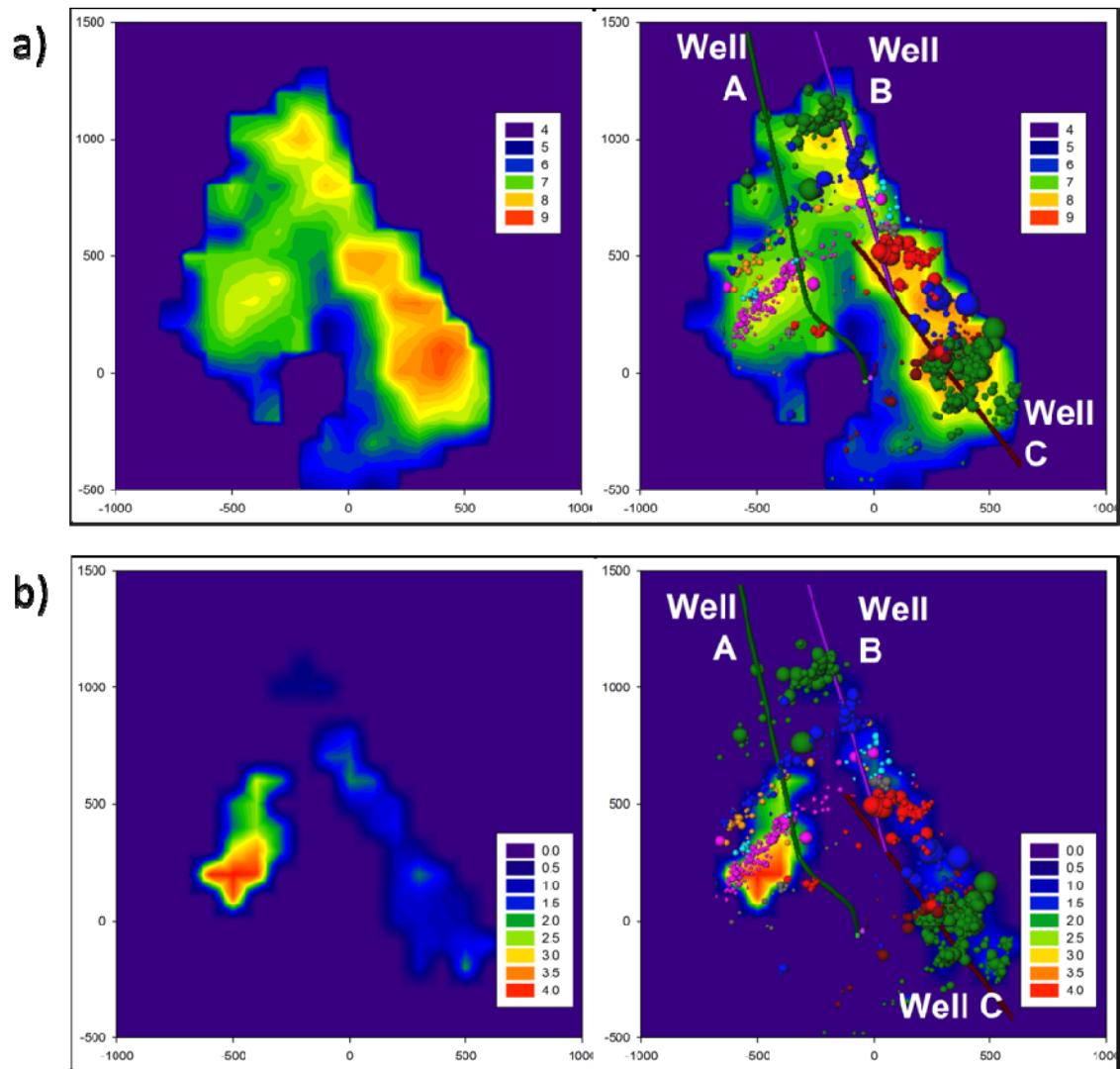
Figure 4.2. Contours of the a) seismic moment density and b) *b*-values illustrating the microseismic source strength and slope of the frequency-magnitude relationship respectively. The events along Wells B and C are consistent with fault activation while the events SW of Well A are consistent with conventional hydraulic fractures (From Maxwell et al., 2011).

In addition, composite focal mechanisms were computed by Maxwell et al. (2011) to determine the average failure mechanism associated with the microseismicity (e.g., Rutledge et al., 2004). The analysis performs a best fit between the observed radiation patterns from groups of events and the theoretical radiation pattern of a single shear

deformation event. Due to the directionality of the source mechanism, S- to P-wave amplitude ratios vary as a function of azimuth with respect to the receiver depending on the orientation of the slip plane. Therefore, analysis of the composite focal mechanisms can be performed to reveal insights into the average mode of failure for the microseismic event clusters.
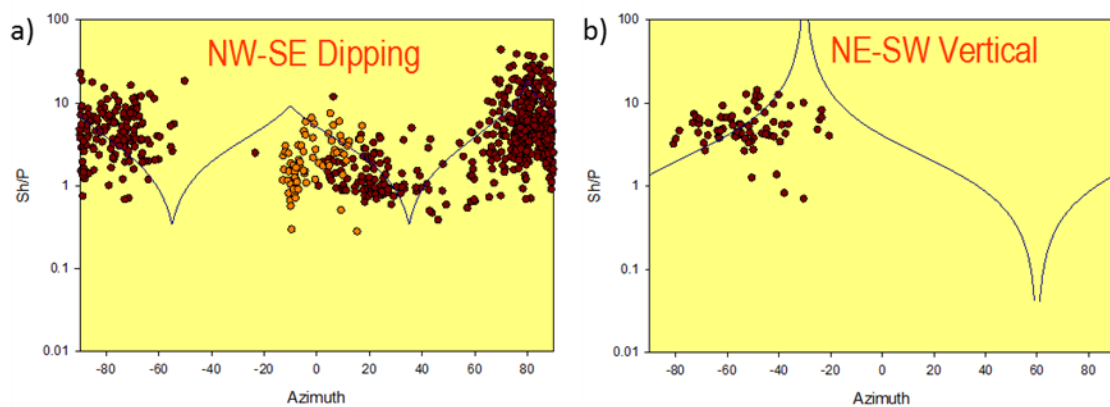
Figure 4.3. Composite focal mechanisms showing the observed S- to P-wave amplitude ratios and modeled radiation patterns, indicating the average failure mechanism for the two event clusters defined by the different *b*-values corresponding to a) fault activation and b) hydraulic fractures (From Maxwell et al., 2011).

Figure 4.3 shows the composite focal mechanisms for the two event clusters defined by the different *b*-values corresponding to fault activation and hydraulic fractures. The events SW of Well A are best modeled by a NE-SW strike-slip mechanism along the expected fracture orientation orthogonal to the regional minimum horizontal stress direction. The events along Wells B and C are best modeled by a NW-SE dip-slip mechanism orthogonal to the expected fracture orientation but are consistent with the regional thrust faults in the area, further supporting the notion of fault activation.

These results clearly indicate a considerable change in the stress field over the stimulation region. SW of Well A, failure occurs under a strike-slip faulting stress regime, where the vertical stress is the intermediate principal stress. Along the length of Wells B and C, failure occurs under a thrust faulting stress regime, where the vertical stress is the minimum principal stress. The question then arises as to what is the underlying mechanism responsible for the observed changes in the stress field. The current hypothesis is associated with the regional deformation where the stress variations result from mechanical alterations in the rock mass associated with tectonic loading.
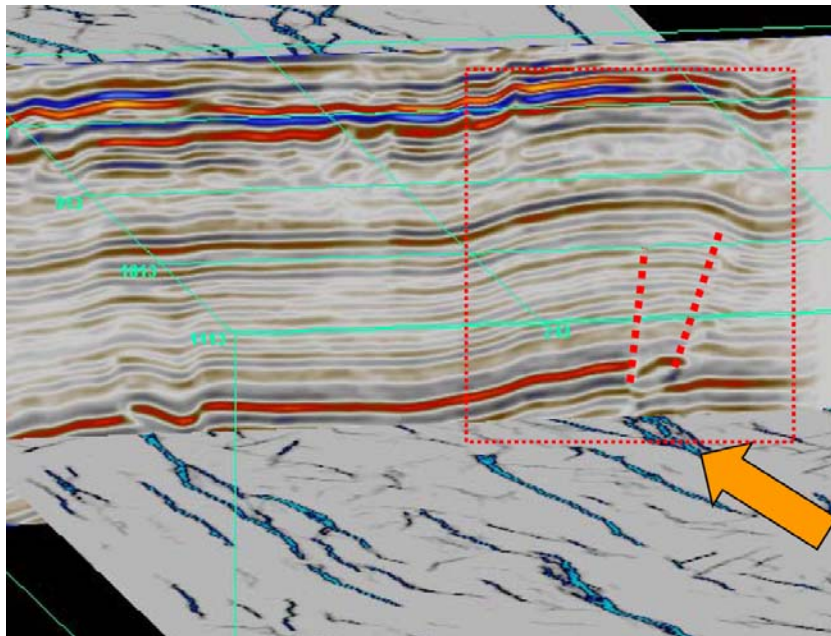
Figure 4.4. Seismic section that shows the presence of thrust faults below the Montney indicated by the arrow and the corresponding structure above in the zone of interest where pre-rupture faults can exist.

Figure 4.4 shows a seismic image illustrating the structural deformation throughout the section. Reflector displacement that corresponds to faulting is observed deeper in the

section but die out as it extends up into the Montney. The faulting however creates structures in the Montney that correspond to deformation prior to brittle failure and the formation of a discrete fault plane, where pre-rupture faults can exist. The following investigates this hypothesis through consideration of the changes in mechanical properties throughout the deformation process and the associated response of the mechanically altered material.

4.3 Failure process

4.3.1 The stress-strain curve

The process of failure can be modeled in the laboratory in which rock samples are loaded to investigate the deformation at various points throughout their stress history. Consider a typical stress-strain curve for a rock specimen subjected to uniaxial compression with a constant lateral confining stress as in Figure 4.5. The curve can be divided conceptually into three regions where the rock exhibits elastic, ductile and brittle behavior.
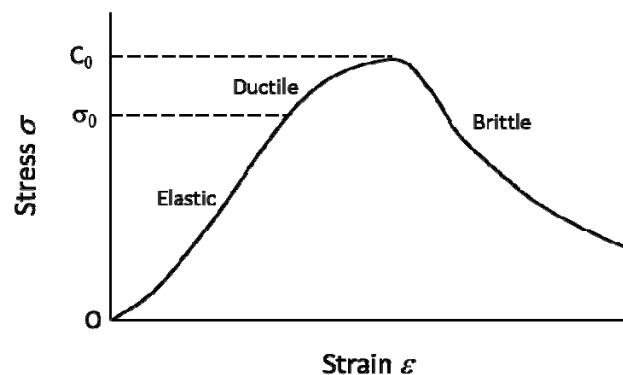
Figure 4.5. Stress-strain curve illustrating the elastic, ductile and brittle regions of a rock specimen subjected to uniaxial compression under a constant lateral confining stress.

The elastic regime is characterized by the linear region of the curve. Loading and unloading in this region will follow the same path along the stress-strain curve and will not produce irreversible changes in the structure or material properties of the rock. The transition from elastic to ductile behavior occurs at a point known as the yield stress, σ_0, of the material. The ductile regime is then characterized by a gradual decrease in the slope of the curve until a value of zero is reached. In this region, the transverse strains begin to grow in magnitude at a much faster rate than the axial strain. This means that an incremental increase in the axial compressive stress results in an incremental increase in the volume, a phenomenon known as dilatancy. The increase in volume under an additional compressive stress can be attributed to the formation and extension of microcracks oriented parallel to the direction of the maximum principal stress. Irreversible changes to the structure and material properties occur throughout this region and successive loading and unloading cycles will follow different paths along the stress-strain curve, resulting in changes to the effective elastic properties. The point at which the slope of the stress-strain curve is zero marks the transition from ductile to brittle behavior and is known as the uniaxial compressive strength, C_0, of the material. The brittle regime is then characterized by a negative slope in the stress-strain curve where failure occurs throughout this region as a continuous process in which the material physically deteriorates.

4.3.2 The in-situ formation of microcracks

Triaxial compression tests are typically performed under the condition of a constant lateral confining stress, where the lateral expansion of the specimen is unrestricted. One

can imagine however that the lateral confining stress in-situ is a function of the surrounding material, which exhibits a finite stiffness. As a rock mass deforms laterally, the adjacent rock would respond by increasing the lateral confining stress with increasing lateral strain, therefore inhibiting localized lateral expansion.
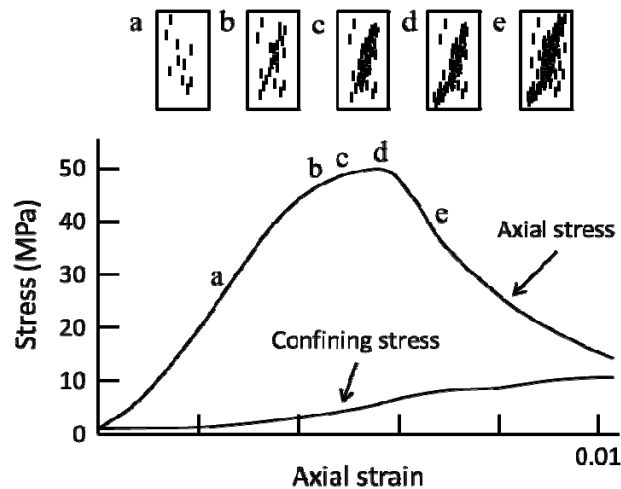
Figure 4.6. Schematic representation of the experiment performed by Hallbauer et al. (1973) illustrating the mechanical alterations in a rock specimen at various points along the stress-strain curve (Adapted from Jaeger et al., 2007).

Hallbauer et al. (1973) performed a triaxial compression test that more closely represents the conditions in-situ to characterize the physical changes to a rock sample throughout the failure process. Using an annealed copper tube and a fixed fluid volume in a triaxial test cell, they were able to provide stiffness to the confinement of the specimen. The samples were loaded to predetermined points along the stress-strain curve to investigate the structural changes that occur as a result of loading. Thin sections were subsequently prepared at the various stages of loading to illustrate the mechanical alterations undergone during the deformation process. Figure 4.6 illustrates the results of

67

their experiment. The structural changes observed in the specimen consisted of microcracks that formed throughout the deformation process. The orientation of the microcracks is parallel to the direction of maximum principal stress, which was applied along the axis of the cylindrical samples. In the elastic regime (region a in Figure 4.6), slight hysteresis occurred where the microcracks were distributed uniformly throughout the sample. In the ductile regime (regions b, c, and d in Figure 4.6), the density of microcracks increased dramatically as the axial stress approached the ultimate strength of the specimen, where the distribution of microcracks begins to concentrate near the center of the specimen along a plane. As loading approached the ultimate strength of the specimen and into the brittle regime (region e in Figure 4.6), the microcracks coalesce to form a discrete fracture plane.

In our study of pre-rupture faults, the region of interest is the ductile regime of the stress-strain curve, where the formation of aligned microcracks alters the mechanical properties of the rock mass and changes the effective elastic properties. In addition, we assume the microcracks are hydraulically isolated prior to coalescing to form a discrete fracture plane. To investigate the associated properties of the mechanically altered material, we use Hudson's penny-shaped crack model (1981), which provides expressions for the effective elastic stiffness parameters associated with aligned penny-shaped inclusions embedded in an isotropic background medium. For simplicity, we consider the case of dry cracks where the effective elastic stiffness parameters are a function of the crack density, ε and the Lamé parameters, λ and μ of the background medium (Appendix A).

4.4 Reflectivity response

Consider a schematic representation of the Montney structure as shown in Figure 4.7. As the underlying thrust faults create the structure in the zone of interest, microcracks could be present as a result of deformation prior to brittle failure, representing a pre-rupture fault. Assuming the microcracks were formed during the development of the thrust faults, they would lie in the horizontal plane as the maximum principal stress is horizontal in a thrust faulting stress regime. Clusters of microcracks would then change the effective elastic properties of the medium.
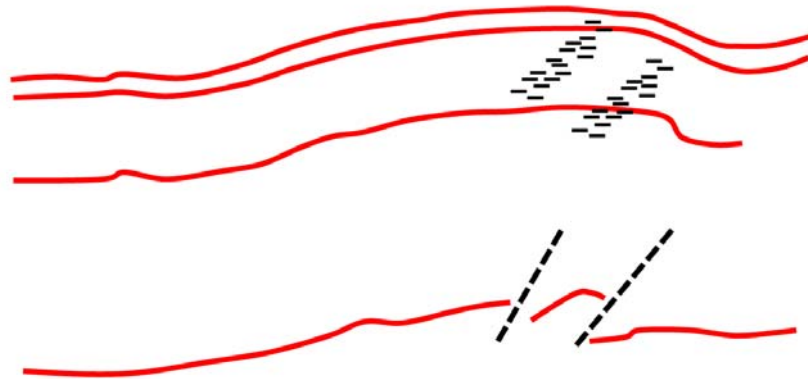
Figure 4.7. Schematic representation of the Montney structure illustrating the possible presence of pre-rupture faults consisting of microcracks that lie in the horizontal plane. At a reflection interface where microcracks exist, the reflection coefficient changes relative to the unaltered background.

The normal incidence reflection coefficient across an interface where microcracks exists is given by

$$R = \frac{v_2^{(eff)}\rho_2 - v_1^{(eff)}\rho_1}{v_2^{(eff)}\rho_2 + v_1^{(eff)}\rho_1},$$ (4.1)

where ρ is the density and $v^{(eff)}$ is the effective vertical P-wave velocity, and is given by

$$v^{(eff)} = \sqrt{\frac{C_{33}^{(0)}(\lambda,\mu) + C_{33}^{(1)}(\lambda,\mu,\varepsilon)}{\rho}} \ . \tag{4.2}$$

In equation 4.2, $C_{33}^{(0)}$ is the elastic stiffness parameter corresponding to the vertical P-wave velocity for the isotropic background and $C_{33}^{(1)}$ is the first order perturbation due to the inclusion of the penny-shaped cracks (Appendix A). In the region where cracks exist, ε is finite, resulting in a change in vertical P-wave velocity and the normal incidence reflection coefficient relative to the unaltered background. In addition, since the geometry associated with the cluster of microcracks forms a planar feature, amplitude changes in the seismic image can be identified using the ant tracking algorithm as discussed in §3.3.1. Here, we are interested in the subtle changes in reflection amplitudes that exhibit fault-like features. Figure 4.8 shows the ant tracking results for the zone of interest. The stronger events highlighted in blue correspond to edges of a structural feature and represent the fold axial planes. However, the weaker events as outlined represent subtle changes in the reflection amplitudes that exhibit spatial planarity consistent with the regional thrust faults. Therefore, these features represent the possible presence of pre-rupture faults capable of affecting the hydraulic fracture response.
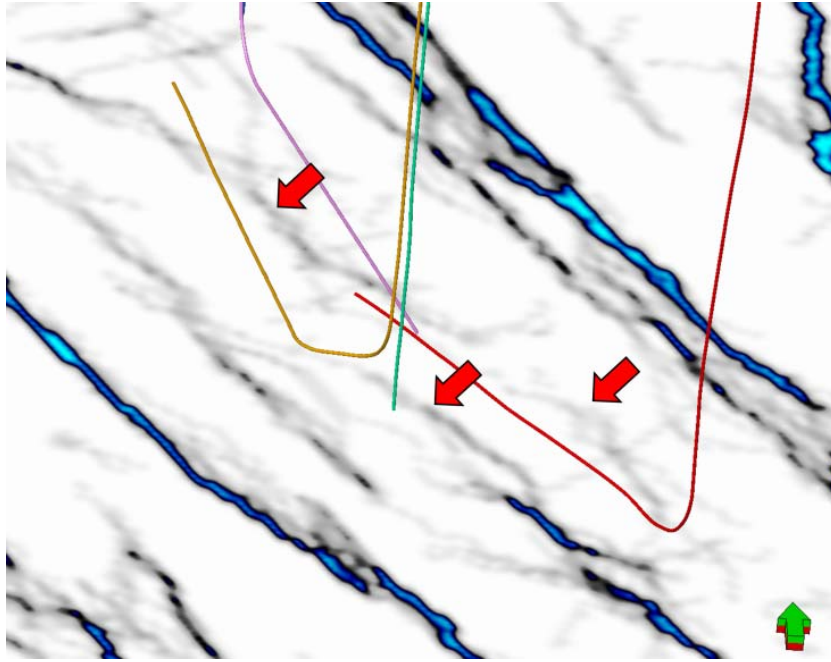
Figure 4.8. Ant tracking image showing the presence of subtle amplitude changes that exhibit spatial planarity consistent with the regional thrust faults, indicating the possible presence of pre-rupture faults (Modified from Norton et al., 2010).

4.5 An effective stress model for pre-rupture faults

To investigate the effective stress field experienced by pre-rupture faults, consider an infinitely thin crack embedded in an isotropic homogenous background as illustrated by the solid blue line in Figure 4.9. The crack is subjected to a uniform normal traction, p, applied to its faces, as would be the case for the pressure exerted by a pore fluid. Sneddon (1946) derived the displacement for the crack surface in a direction normal to its plane given by

$$w(r) = \frac{2(1-\nu)pa}{\pi\mu}\sqrt{1-(r/a)^2} \ , \tag{4.3}$$

71

where ν and μ are the Poisson's ratio and shear modulus of the isotropic background medium respectively, a is the radius of the crack and r is the radial distance from the center of the crack in the crack plane.
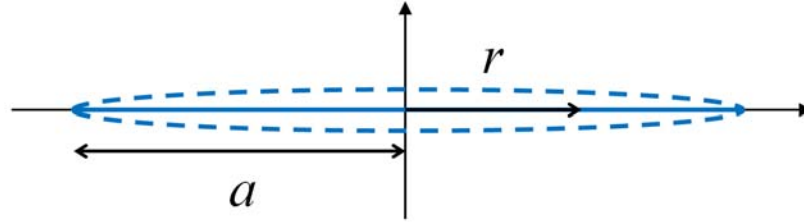
Figure 4.9. Schematic representation of an infinitely thin crack (solid line) and the associated displacement (dashed line) upon the application of a uniform normal traction, such as that would be applied by a pore fluid.

The pressurization of the crack results in an opening displacement that is greatest in the center and zero at the crack edge as illustrated by the dashed blue line in Figure 4.9. The excess elastic strain energy due to a pressurized crack can be calculated as in Jaeger et al. (2007) by solving

$$W_{crack} = \frac{1}{2} \int_{2A} pw dA = \int_0^{2\pi} \int_0^a \frac{2(1-\nu)p^2 a}{\pi \mu} \sqrt{1-(r/a)^2}\, r dr d\theta , \qquad (4.4)$$

which yields

$$W_{crack} = \frac{4(1-\nu)p^2 a^3}{3\mu} . \qquad (4.5)$$

Note that the pressure and displacement in equation 4.4 are those that exist at equilibrium and do not refer to the values during the loading process (Jaeger et al., 2007). As the initial surface of the crack lies entirely in a two dimensional plane, the state of loading considered here is equivalent to the case of a far-field hydrostatic loading of magnitude p

(Jaeger et al., 2007). Consequently, no additional elastic strain energy arises for far-field principal stresses that are parallel to the plane of the crack (Sack, 1946). This suggests that the strain associated with a pressurized crack act only in a direction normal to the crack face.

Now consider a medium with a volume, V, containing N number of cracks. The resulting excess elastic strain energy density can be obtained by the multiplication of equation 4.5 by N/V. In addition, using the definition of crack density given by

$$\varepsilon = \frac{Na^3}{V},$$

(4.6)

an expression for the excess elastic strain energy density as a function of crack density can be obtained and is given by

$$W = \frac{4(1-\nu)p^2\varepsilon}{3\mu}.$$

(4.7)

We seek an expression for the effective stress due to the presence of aligned penny-shaped cracks subjected to a pore pressure, p. By assuming that the opening displacement is small, the normals to the crack surface lie along a single axis. The resulting stress exerted by the pore fluid is uniaxial and act only in a direction normal to the crack face. Differentiation of equation 4.7 with respect to p then yields the excess strain as a result of the pressurized cracks and is given by

$$e^{(excess)} = \frac{\partial W}{\partial p} = \frac{8(1-\nu)p\varepsilon}{3\mu},$$

(4.8)

where it is finite only along the direction normal to the crack face. Subsequently, the corresponding components of the excess stress can be obtained using Hooke's law given by

$$\begin{bmatrix} \sigma_{11}^{(excess)} \\ \sigma_{22}^{(excess)} \\ \sigma_{33}^{(excess)} \\ \sigma_{23}^{(excess)} \\ \sigma_{13}^{(excess)} \\ \sigma_{12}^{(excess)} \end{bmatrix} = \begin{bmatrix} C_{11} & C_{12} & C_{13} & 0 & 0 & 0 \\ C_{12} & C_{22} & C_{23} & 0 & 0 & 0 \\ C_{13} & C_{23} & C_{33} & 0 & 0 & 0 \\ 0 & 0 & 0 & C_{44} & 0 & 0 \\ 0 & 0 & 0 & 0 & C_{55} & 0 \\ 0 & 0 & 0 & 0 & 0 & C_{66} \end{bmatrix} \begin{bmatrix} e_{11}^{(excess)} \\ e_{22}^{(excess)} \\ e_{33}^{(excess)} \\ e_{23}^{(excess)} \\ e_{13}^{(excess)} \\ e_{12}^{(excess)} \end{bmatrix}, \qquad (4.9)$$

where the C_{ij}'s represent the effective elastic stiffness parameters as given by Hudson's penny-shaped crack model (1981) in Appendix A. The resulting effective stresses are then given by

$$\sigma_{ij}^{(eff)} = \sigma_{ij} - \sigma_{ij}^{(excess)}. \qquad (4.10)$$

Since only one normal excess strain (e.g., $e_{ij}^{(excess)}$ for $i=j$) is finite due to a set of aligned pressurized cracks, we obtain three normal excess stresses. For cracks in the x_1-x_2 plane, the excess stresses are given by

$$\sigma_{11}^{(excess)} = \frac{8C_{13}(1-v)\varepsilon}{3\mu} p = \beta_{13} p, \qquad (4.11)$$

$$\sigma_{22}^{(excess)} = \frac{8C_{23}(1-v)\varepsilon}{3\mu} p = \beta_{23} p, \qquad (4.12)$$

and

$$\sigma_{33}^{(excess)} = \frac{8C_{33}(1-v)\varepsilon}{3\mu} p = \beta_{33} p. \qquad (4.13)$$

The parameters β_{ij} in equations 4.11 to 4.13 are analogous to the Biot-Willis parameter, α, which represents the proportion of fluid pressure which will produce the same strains as the total stress (Biot and Willis, 1957). In most porous rocks, the pressure applied inside the pores will result in a smaller strain on the total rock volume than the same pressure applied on the total rock volume, therefore α and β_{ij} will take on values that are

typically less than one. Furthermore, in equations 4.11 to 4.13, ν and μ represent the background medium and C_{ij}'s represent the effective medium, therefore these are analogous to the solid phase and saturated moduli of Biot and Willis (1957) respectively.

4.6 Discussion

Given the above description of the failure process and an effective stress model for a medium containing penny-shaped cracks, we can proceed with the presentation of a model to explain the variability of the stress field in the stimulation region.

During the formation of the regional thrust faults, it is likely that there exists a complete range of rocks at various stages in the deformation process. The area along the length of Wells B and C where fault activation occurred is hypothesized to be loaded to the ductile region of the stress-strain curve, representing a pre-rupture fault. Since the maximum and minimum principal stress directions in a thrust faulting stress regime are horizontal and vertical respectively, the microcracks that form as a result of loading lie in the horizontal plane. We then model the rock mass as an isotropic medium containing spherical pores and aligned penny-shaped cracks in the horizontal plane. In a strike-slip faulting stress regime, $\sigma_H^{(eff)} > \sigma_V^{(eff)} > \sigma_h^{(eff)}$ and in a thrust faulting stress regime, $\sigma_H^{(eff)} > \sigma_h^{(eff)} > \sigma_V^{(eff)}$, where the subscripts V, H and h denote the vertical and maximum and minimum horizontal stresses respectively. Therefore, we are interested in the relative magnitudes of $\sigma_V^{(eff)}$ and $\sigma_h^{(eff)}$ as a function of crack density. The corresponding effective vertical stress is given by

$$\sigma_V^{(eff)} = \sigma_V - \beta_{33} p, \tag{4.14}$$

and the effective minimum horizontal stress is given by

$$\sigma_h^{(eff)} = \sigma_h - \beta_{13}p. \tag{4.15}$$

For the following numerical calculations, we assume that the cracks are dry. To calculate the stresses, we use a pressure gradient of 25 kPa/m and the average measured closure stress value of 23 kPa/m for the vertical and minimum horizontal stresses respectively. To calculate β_{lj}, average values in the Montney were used to represent the isotropic background where the P- and S-wave velocities and density were taken to be 4750 m/s, 2800 m/s and 2650 kg/m³ respectively. The pore pressure was taken to be 30 MPa. Figure 4.10 shows the effective vertical and minimum horizontal stress as a function of crack density. Note that the effective vertical stress decreases at a faster rate relative to the effective minimum horizontal stress. At a crack density of approximately 0.035, a cross over from a strike-slip to thrust faulting stress regime occurs. The presence of a pre-rupture fault changes the pore pressure response and ultimately the stress regime experienced by the rock mass. Therefore, we attribute the variable hydraulic fracture response to the presence of aligned cracks and its associated response to a uniform normal traction applied by a pore fluid.
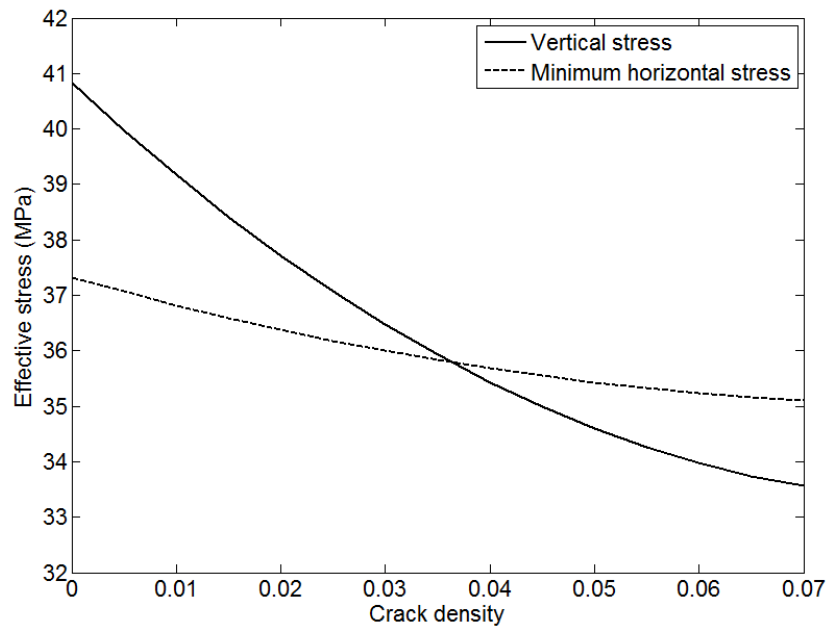
Figure 4.10. The effective minimum horizontal and vertical stresses as a function of crack density. A cross over from a strike-slip to thrust faulting stress regime occurs at a crack density of approximately 0.035.

4.7 Chapter summary

The large variability in the hydraulic fracture response of a tight gas reservoir was investigated through a micromechanical model representing a pre-rupture fault. Laboratory experiments demonstrate the formation of aligned microcracks throughout the deformation process and therefore, a penny-shaped crack model was used to investigate the associated response of the mechanically altered material. Due to the planarity of the deformation zone associated with pre-rupture faults, these features were extracted from the seismic image using a pattern recognition algorithm that identifies planar features. In addition, an effective stress model was presented to investigate the response of such media to the pressure applied by a pore fluid. The proposed effective stress model predicts an excess strain that acts only in a direction normal to the crack face. For the

77

case of the hypothesized pre-rupture fault along Wells B and C, this effect caused a cross over from a strike-slip to thrust faulting stress regime, resulting in the observed hydraulic fracture behavior.

Chapter Five

4D analysis of hydraulically induced fractures

5.1 Introduction

In this chapter, we present a methodology to evaluate fluid mobility in the stimulated zone for a hydraulic fracture treatment in the Horn River gas shales of NE British Columbia, Canada. This study builds upon the work of Goodway et al. (2012), where an integrated study was performed to predict and characterize well performance through advanced quantitative interpretation methods for reservoir characterization. Their study detailed the workflow from which "sweet spots" were identified through geomechanical and rock property estimation from 3D seismic data. Furthermore, the microseismicity associated with the hydraulic fracture treatment and 4D seismic were used to evaluate the extent of the SRV, which provides a tool to confirm and calibrate the predictions of the seismic reservoir characterization study. Here, we investigate an observed attenuation response in the 4D seismic that was hypothesized to be the result of squirt flow effects, which can be used as a proxy for permeability.

We begin with an overview of the squirt flow phenomenon in fractured porous media and the corresponding frequency dependent attenuation response. Subsequently, we present the interpretation of the induced microseismicity and 4D seismic anomalies to determine the SRV and the 4D attenuation analysis for permeability estimates to corroborate information acquired from independent sources of data.

79

5.2 Squirt flow in mesoscale fractures

Wave-induced fluid flow between open fractures in a poroelastic background was discussed by Brajanovski et al. (2005), where they modeled the fractured medium as a porous background with highly compliant layers that represent fractures. In their description of the phenomenon, mesoscale fractures were considered, where mesoscale means small compared to the seismic wavelength but much larger than the size of individual grains and pores. For the present study, the assumption of mesoscale fractures is reasonable as the hydraulically induced fractures are not directly resolvable seismically and the grain and pore sizes in shales are much smaller.

For the case of liquid-filled fractures that are not hydraulically isolated, the passage of a seismic wave induces a pore pressure gradient in the medium. To equilibrate pressure, fluid diffusion occurs across the interface between the layers representing the background and fractures, where this can be regarded as two coupled diffusion processes (Gurevich et al., 2007). As the diffusion characteristics associated with the background and fractures are different, superposition results in a frequency dependence of the elastic parameters. This ultimately gives rise to velocity dispersion and attenuation of the seismic energy, which can be used to provide an indication for fluid mobility or the permeability in the medium.

The dynamic-equivalent saturated P-wave modulus for the system as discussed is given by (Brajanovski et al., 2005)

$$\frac{1}{c_{11}^{sat}} = \frac{1}{C}\left[1 + \frac{(C-\alpha M)^2}{CL} \frac{\Delta_N}{1-\Delta_N+\Delta_N\sqrt{i\Omega}\cot\left(\frac{C}{M}\sqrt{i\Omega}\right)}\right], \qquad (5.1)$$

where

$$L = K + \frac{4}{3}\mu , \tag{5.2}$$

$$C = L + \alpha^2 M , \tag{5.3}$$

$$M = \frac{K_g}{\left(1 - \dfrac{K}{K_g}\right) - \phi\left(1 - \dfrac{K_g}{K_f}\right)} , \tag{5.4}$$

and

$$\Omega = \frac{\omega\eta H^2 M}{4\kappa CL} , \tag{5.5}$$

where the quantity, Ω, is known as the normalized frequency, K, K_g and K_f are the bulk

modulus of the dry matrix, solid grain and fluid respectively, μ is the shear modulus, α is

the Biot-Willis coefficient, ϕ is porosity, ω is the frequency, H is the fracture spatial

period, Δ_N is the normal fracture weakness (Schoenberg and Sayers, 1995), κ is the

permeability and η is the dynamic viscosity. The effect of fluid motion between fractures

and pores gives rise to complex elastic stiffness coefficients that result in a frequency

dependent response. The corresponding attenuation is given by

$$\frac{1}{Q} = \frac{\mathrm{Im}\left(c_{11}^{sat}\right)}{\mathrm{Re}\left(c_{11}^{sat}\right)} , \tag{5.6}$$

where Q is the quality factor. Figure 5.1 shows the attenuation as presented by

Brajanovski et al. (2005) for a constant normal fracture weakness of 0.2 and different

background porosity values. The wave-induced fluid flow between fractures and pores

exhibits an attenuation response that is characteristic of a relaxation phenomenon

(Brajanovski et al., 2005) where the attenuation peaks at some frequency and falls off thereafter.
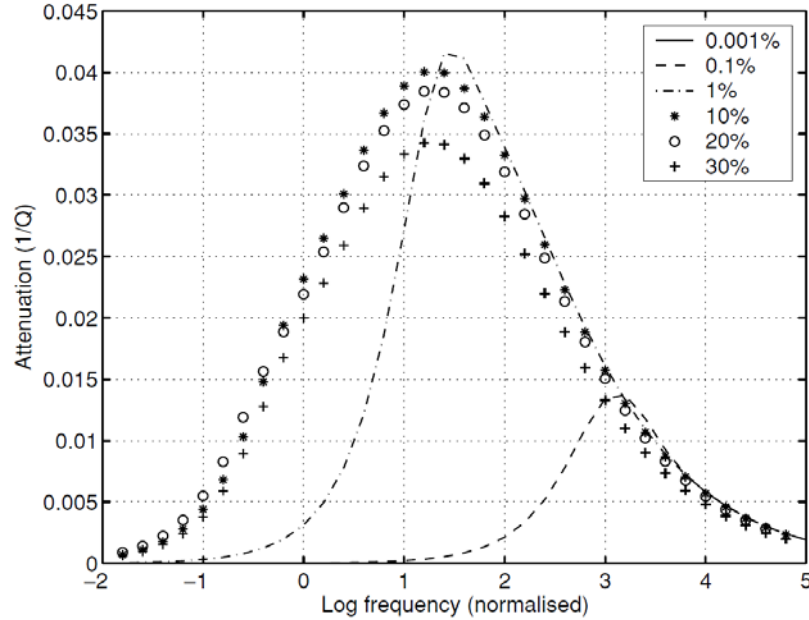
Figure 5.1. Attenuation response for mesoscale fractures in a porous background for a constant normal fracture weakness of 0.2 and different background porosity values (From Brajanovski et al., 2005).

The P-wave modulus given by equation 5.1 represents the response for an applied stress normal to the fracture plane, and is therefore only applicable for plane waves propagating along the fracture normal. However, due to the source-receiver offsets in the data acquisition, plane-wave components should exist that are normal to the fracture plane for various fracture geometries. Therefore, we expect a finite attenuation response despite the non-ideal experimental setup. In addition, for a quantitative description of the attenuation response, we require knowledge of parameters such as the fracture dimensions and a fluid mobility parameter, which are unknown at present. Therefore, we

are restricted to a qualitative analysis to evaluate the attenuation response and hence the estimation of permeability in the stimulated zone.

5.3 Microseismic and 4D seismic analysis

The induced microseismicity as a result of the hydraulic fracture treatment was recorded to determine the extent of the SRV. Figure 5.2 shows the microseismic event locations overlaid on a curvature attribute map illustrating the location of a fault cutting through the well pad. For the completion of stages located near the fault, a lack of microseismic events was observed in the immediate vicinity as outlined in yellow. However, microseismic events appeared at the toe of the wells suggesting a deflection of energy that re-stimulates the NW end of the pad.
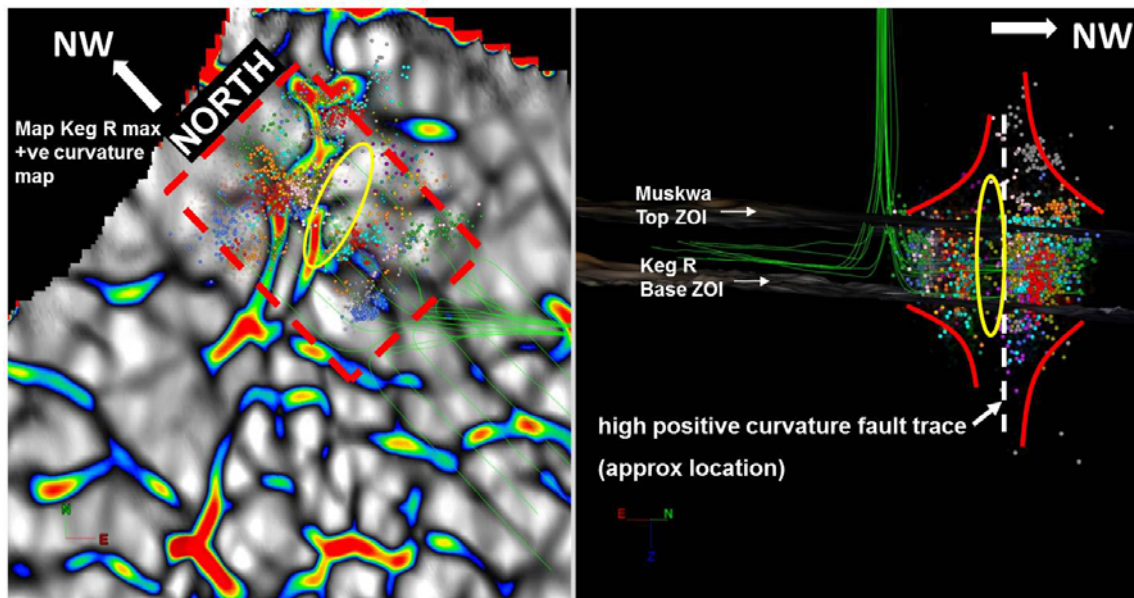
Figure 5.2. Microseismic event locations overlaid on a curvature attribute map illustrating the location of a fault cutting through the well pad (From Goodway et al., 2012).

Figure 5.3 shows the 4D amplitude and traveltime anomalies for the stimulated interval. The two properties demonstrate a consistent 4D anomaly at the toe of the wells where the apparent re-stimulation created a significantly damaged zone that was detectable seismically. In addition, the anomalies appear to be bounded by the curvature event and in conjunction with the microseismic observations, suggest that fluid was transported through the fault but resulted in little change in the fault zone.
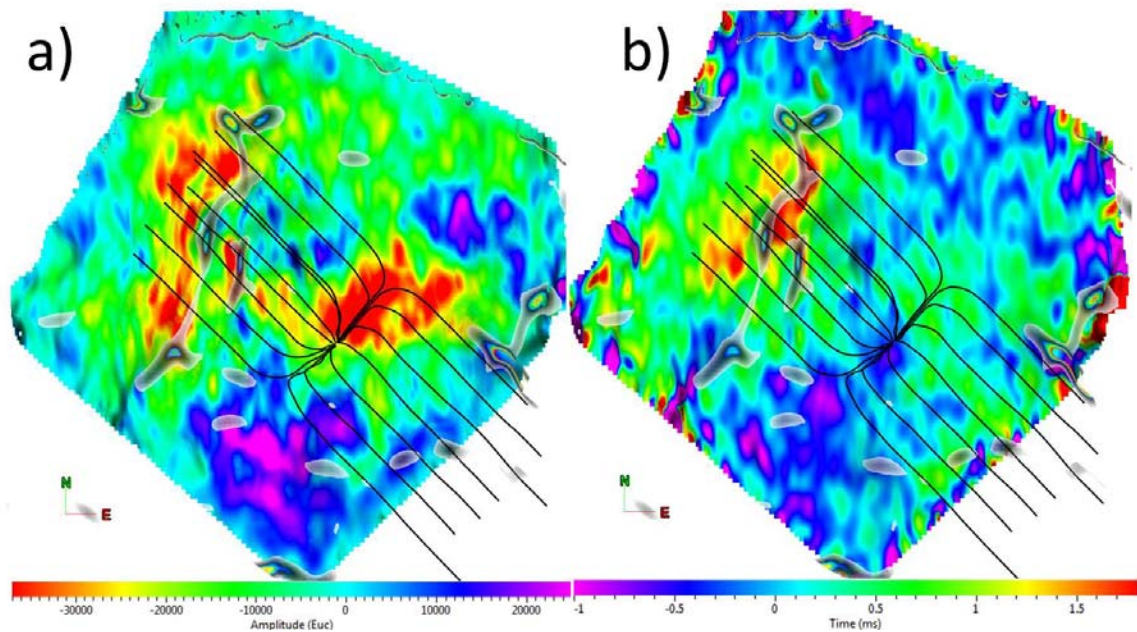
Figure 5.3. Map view of the 4D a) amplitude and b) traveltime anomalies associated with the hydraulic fracture treatment with the well trajectories overlaid. The curvature is also overlaid to indicate the location of the fault (From Goodway et al., 2012).

5.4 4D attenuation analysis

To provide an indication for fluid motion in the stimulated zone, we perform a spectral analysis to investigate the presence of attenuation effects as discussed above.
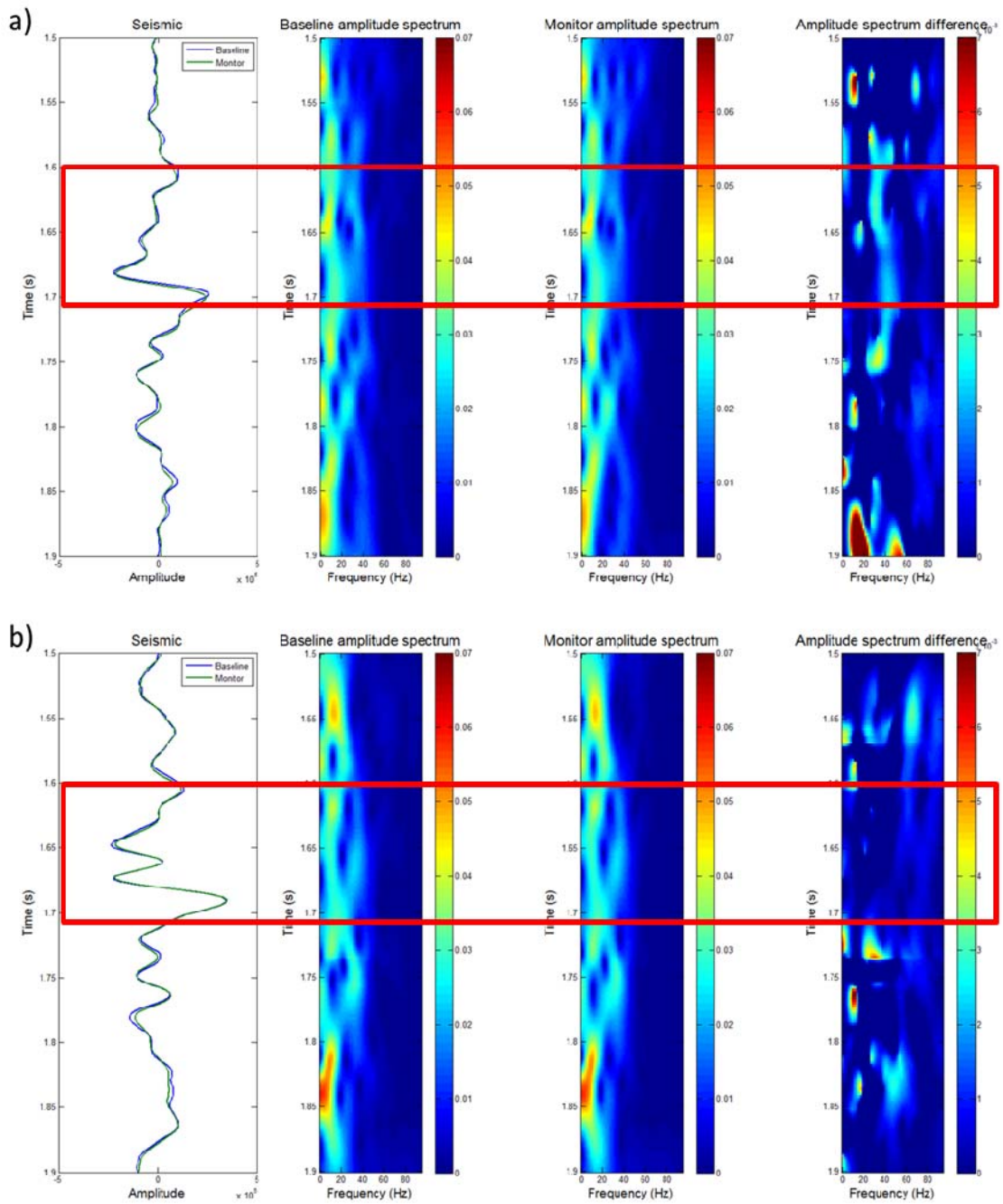
Figure 5.4. Time variant amplitude spectrum for an area a) with and b) without stimulation where attenuation effects are observed in a) throughout the reservoir interval at approximately 1.6 to 1.7 seconds as outlined.

The monitor survey for the 4D analysis was acquired during the completions program where the hydraulic fracturing fluid has not yet been recovered. As the original state of the reservoir was completely gas saturated, even existing fractures that are permeable will not produce the attenuation effects due to the motion of a liquid phase between fractures and pores. Therefore, the baseline survey provides a reference to detect any attenuation effects in the monitor survey.

Figure 5.4 shows time-variant amplitude spectra and their difference for a single trace extracted from the baseline and monitor surveys in an area with and without stimulation, where the reservoir interval is approximately between 1.6 and 1.7 seconds as outlined. In the area without stimulation, a minimal amplitude difference is observed throughout the reservoir interval. Conversely, in the area with stimulation, a finite amplitude difference is observed that extends throughout the reservoir interval and is isolated to a specific frequency band.
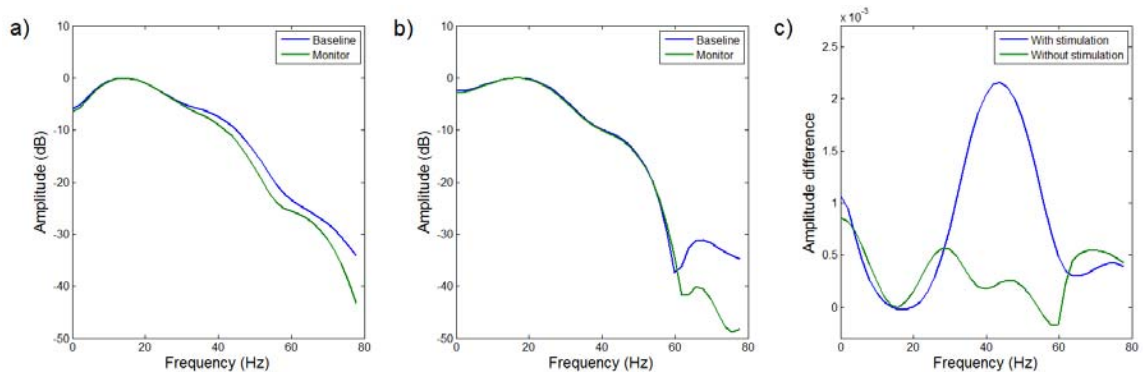
Figure 5.5. Time slice through the time variant spectrum illustrating the amplitude response for an area a) with and b) without stimulation and c) the amplitude spectrum difference between the baseline and monitor surveys.

Figure 5.5 shows a slice through the time-variant spectra in the reservoir interval where these effects are more clearly seen. The difference amplitude spectrum demonstrates a decrease in amplitude that peaks at some frequency and falls off thereafter.

To illustrate the areal extent of the attenuation response, a spectral decomposition was performed for the 4D volumes windowed around the reservoir interval. Figure 5.6 shows the difference in the 35 Hz spectral component between the baseline and monitor surveys, where the hot colors represent areas of increased attenuation and hence, fluid mobility within the stimulated zone.
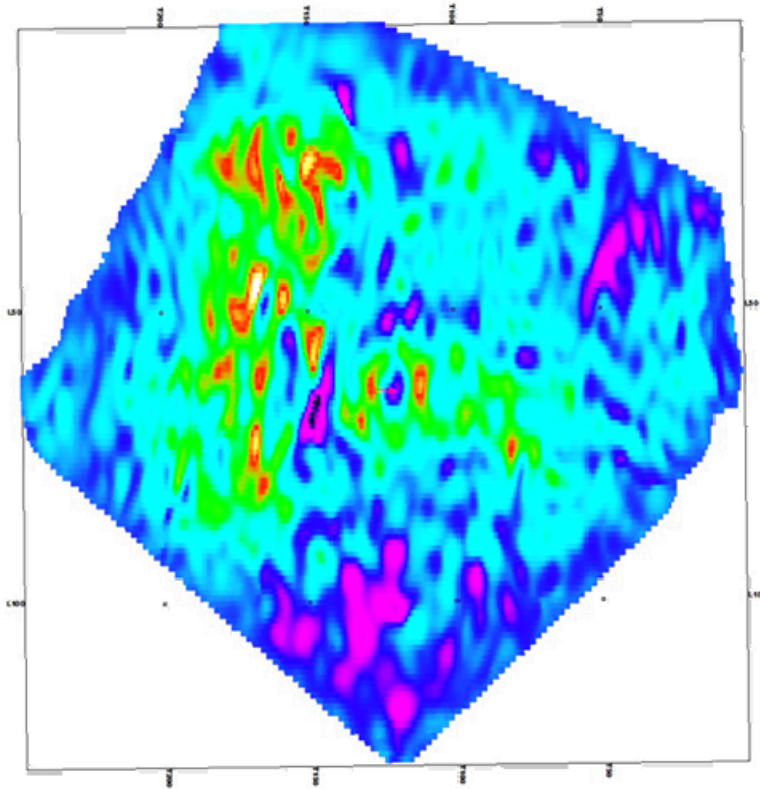
Figure 5.6. Map illustrating the areal extent of the 4D attenuation anomalies suggesting fluid mobility in the stimulated zone. Also note the attenuation trend that tracks the curvature event outlining the location of the fault.

The attenuation response is consistent with the amplitude and traveltime anomalies which are concentrated near the toe of the wells, confirming the extent of the SRV. In addition, the spectral-difference map exhibits an attenuation trend that tracks the curvature event outlining the location of the fault. As suggested by the microseismic observations and seismic amplitude and traveltime anomalies, energy is deflected towards the toe of the wells through the fault. The attenuation response therefore, is consistent with the interpretation of a permeable fault, which served as a conduit for the transport of fluid to re-stimulate the NW end of the well pad.

5.5 Chapter summary

Estimates of permeability in hydraulically induced fractures were performed through spectral analysis of a 4D seismic survey. Estimates are based on theoretical predictions that the effect of fluid mobility results in a frequency dependent attenuation response. Comparison of time-variant amplitude spectra for baseline and monitor surveys shows a bandlimited spectral anomaly in the reservoir zone consistent with theoretical expectations. In addition, the results of the attenuation analysis were consistent with microseismic observations and 4D seismic amplitude and traveltime anomalies, suggesting that fluid was transported through the fault, diverting energy from the hydraulic fracture treatment to re-stimulate the NW end of the well pad.

Chapter Six

Conclusions

An investigation into subsurface fracture phenomena as it pertains to unconventional resource exploration and development was undertaken in this thesis. This includes the presentation of methods for the inference of naturally occurring fracture systems and the evaluation of the hydraulic fracture response, especially in the vicinity of fault related features.

In chapter two, we presented an azimuthal AVO inversion methodology to address some outstanding issues regarding conventional azimuthal fracture characterization techniques. These include the estimation of layer properties rather than interface properties, a more general description of the TI reflection problem that allows for arbitrary fracture geometries and the resolution of the 90° ambiguity in the estimation of the symmetry axis azimuth. The proposed methodology is capable of providing improved estimates of subsurface fracture parameters without certain limiting assumptions, therefore reducing the uncertainty associated with fracture characterization studies.

In chapter three, we presented a case study for fracture inference using isotropic analysis techniques. This is applicable for situations where data limitations inhibit the use of azimuthal analysis. The methodology includes the use of structural attributes extracted from the post-stack seismic image to identify chances in structure and elastic properties estimated from pre-stack seismic data to investigate the changes in elastic properties due to fracturing. The combined interpretation of these results suggests the existence of a

contractional fault-bend fold, where its associated characteristics as identified from seismic analysis are consistent with geological models. Using the proposed methodology, the overall risk is reduced for fracture inference relative to conventional attribute analysis alone.

In chapter four, we presented a micromechanical model to represent a pre-rupture fault and to evaluate the corresponding pore pressure response. This was performed to investigate the large variations observed in the microseismicity associated with the stimulation of a tight gas reservoir. The hypothesized pre-rupture fault causes mechanical alterations in the rock mass, resulting in changes to the reservoir conditions over relatively small distances. Consequently, the effective stress field experienced by the rock mass is altered, affecting the stimulation response to produce unexpected fracture patterns. Using seismic data, subtle changes in the reflection response can be detected and with the use of a pattern recognition algorithm, pre-rupture faults can be identified. Using this information, the hydraulic fracture response in the vicinity of these features can be anticipated to allow for a more effective stimulation program and to mitigate the associated risks.

In chapter five, we used 4D seismic data to investigate the changes in reservoir conditions due to hydraulic fracturing. This was performed to evaluate fluid mobility in the stimulated zone and the extent of the SRV. A band limited attenuation response was identified from the 4D seismic data, which was hypothesized to be the result of squirt flow effects and was used as a proxy for permeability. These results were used to confirm the existence of a permeable fault that diverted hydraulic fracture energy to re-stimulate a specific portion of the reservoir as concluded from microseismic observations.

Furthermore, the results of the attenuation analysis were in agreement with microseismic and 4D seismic amplitude and traveltime anomalies to confirm the extent of the SRV. This study introduces a new methodology using 4D seismic to infer the permeability of the stimulated zone and hence evaluate the success of the stimulation program.

The methods presented to characterize natural fracture systems provide insight into the state of the subsurface for exploration purposes, where reservoir properties can be estimated for subsequent development strategies. Additionally, issues can often arise during the development phase as a result of reservoir heterogeneity and the possible presence of hazards such as faults. Examples of these issues were illustrated through two case studies of hydraulic fracturing, where we investigated the stimulation response using seismic and microseismic data, especially in the vicinity of fault related features that pose a greater risk for development. This analysis was performed in order to anticipate the outcome and mitigate the associated risks of hydraulic fracturing.

We have demonstrated various applications of geomechanical and seismic methods to investigate fracture phenomena for unconventional resource exploration and development. As fractures play a key role in unconventional systems, we must continually improve our methods to detect their presence and evaluate their response to external forces. Despite the progress that is being made, many more questions remain to be answered. However, the results presented here provide small incremental steps forward to achieve our ultimate goal – the pursuit of knowledge to better understand the subsurface environment.

Chapter Seven

Future research directions

Although major strides in the field of fracture characterization have been made in recent years, there remains much more to be accomplished. To date, the various tools used for fracture description are still based on numerous assumptions in an attempt to simplify the problem. The fact still remains that most geophysical problems are not amenable to analytical treatment. However, better approximations are still required for a more accurate description. For example, the scattering coefficients used to calculate the reflectivity response assume weak contrast interfaces and are first order in the changes in elastic properties. While a weak contrast interface is reasonable in most cases, there are situations where this assumption breaks down and higher order approximations are required. For example, this is discussed in Innanen (2012) where higher order corrective terms were derived for isotropic AVO.

In chapter two, we assumed a single set of vertical fractures in the parameterization of the inverse problem. Although the most compliant fracture set should be oriented perpendicular to the minimum horizontal stress as discussed in chapter three, fractures can exist in multiple orientations and would have a finite contribution to the effective elastic properties. Therefore, investigations into the effect of dipping fractures and multiple fracture sets are required for an improved description. Furthermore, estimated fracture parameters must be calibrated to independent data such as formation micro-imager (FMI) logs to confirm their validity.

In chapters four and five, the hydraulic fracturing case studies demonstrated two significantly different responses of fault systems subjected to stimulation. In the first case study, fault activation occurred upon stimulation, resulting in the generation of unexpected fracture patterns. In the second case study, the fault merely served as a conduit for fluid transport. This demonstrates the unpredictability in the response of fault related features and further investigations must be carried out to improve our understanding of this complex phenomenon. Questions that remain to be answered include whether we can distinguish the difference between the two types of faults as discussed and if the estimated elastic properties can provide insight into their state of stress. As it is difficult to measure the actual in-situ stress state of the subsurface, proper estimates of the elastic properties should at least provide the response to external loading, such as that applied by elevated fluid pressures in a hydraulic fracture experiment.

In addition, the study of hydraulic fracturing can benefit from other fields of physics such as non-linear dynamics. Since it is conjectured that water diffusion stimulates fracture propagation throughout a rock mass, the problem can be formulated as a reaction-diffusion system with an evolution equation of the form (e.g., Kolmogorov et al., 1937)

$$\partial_t q = \underline{\underline{D}} \nabla^2 q + R(q), \tag{7.1}$$

where q is the concentration of a single substance and is a function of space and time, $\underline{D}$ is a matrix of diffusion coefficients and R accounts for all local reactions. For the case of hydraulic fracturing, q would represent the fracture concentration or density, $\underline{D}$ would represent the permeability and R would represent an appropriate formulation of crack

93

propagation that could potentially be obtained from fracture mechanics. The solutions, if they exist, can provide new insights into the hydraulic fracturing problem. As this is inherently a multifaceted process consisting of numerous interacting components, an alternate perspective could add value to the understanding of hydraulic fracturing, allowing us to truly appreciate the intricacies of this complex phenomenon.

Furthermore, as briefly mentioned in chapter one, unconventional energy resources include geothermal systems where energy can be harnessed from deep crustal rocks. Although the case studies presented in this thesis are solely related to the hydrocarbon industry, application of the methods for fracture characterization can be extended to include geothermal reservoirs. These include the characterization of natural fracture pathways for heat exchange and the evaluation of the hydraulic fracture response for enhanced geothermal systems (e.g., Kraft el al., 2009).

As we continually strive to further our understanding of subsurface fracture phenomena, we will be able to address the challenges of an ever increasing demand for energy and develop our energy resources in a safe and environmentally responsible manner.

APPENDIX A

Fracture models

Here, we discuss two mathematical models for fractures to evaluate the changes in elastic properties due to fracturing for subsequent analysis of the seismic response. Specifically, we are interested in systems that exhibit a fracture spacing much less than the measurement scale of seismic waves, as fractures at this scale are unresolved by conventional seismic imaging techniques. Therefore, effective medium theories including Hudson's penny-shaped crack model (1981) and the linear slip deformation model of Schoenberg and Sayers (1995) were used to provide a mathematical representation of fractured media. In the following, we provide a brief description and the formulation of these two fracture models.

A.1. Hudson's penny-shaped crack model

Hudson (1981) derived expressions for the representation media containing a series of aligned penny-shaped inclusions as shown in Figure A-1. The effective elastic stiffness parameters of the medium are given by

$$C_{ij} = C_{ij}^{(0)} + C_{ij}^{(1)}, \tag{A-1}$$

where $C_{ij}^{(0)}$ represents the elastic stiffness of the isotropic background and $C_{ij}^{(1)}$ represents the first order perturbation due to the inclusion of the penny-shaped cracks. Here, we consider the case of dry cracks, where C_{ij} is a function of the Lamé parameters,

λ and μ and the crack density, ε. Due to the perturbative derivation, the expressions are only valid for "small" values of crack density.
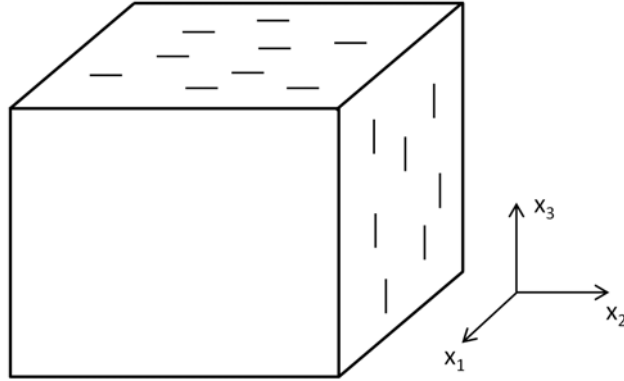
Figure A-1. Schematic of a medium with aligned vertical cracks in the x_2-x_3 plane. This results in a TI medium with five independent elastic stiffness parameters.

Hudson's original formulation includes a second order perturbation term. However, due to the condition of a small crack density, the second order term is negligible and is not considered here. The explicit forms of each independent $C_{ij}^{(1)}$ for the corresponding TI medium with vertical cracks in the x_2-x_3 plane as shown in Figure A-1 are given by (Hudson, 1981)

$$C_{11}^{(1)} = -\frac{4(\lambda + 2\mu)^3}{3\mu(\lambda + \mu)}\varepsilon, \tag{A-2}$$

$$C_{13}^{(1)} = -\frac{4\lambda(\lambda + 2\mu)^2}{3\mu(\lambda + \mu)}\varepsilon, \tag{A-3}$$

$$C_{33}^{(1)} = -\frac{4\lambda^2(\lambda + 2\mu)}{3\mu(\lambda + \mu)}\varepsilon, \tag{A-4}$$

$$C_{44}^{(1)} = 0, \tag{A-5}$$

and

$$C_{55}^{(1)} = -\mu \frac{16(\lambda + 2\mu)}{3(3\lambda + 4\mu)} \varepsilon .$$
(A-6)

To represent arbitrary crack orientations, the coordinate transformations as discussed in chapter two can be applied.

A.2. Linear slip deformation

The linear slip deformation model of Schoenberg and Sayers (1995) models a fractured medium through the sum of compliance matrixes associated with an unfractured background rock and a set of aligned fractures. Assuming a set of rotationally invariant fractures, the effective compliance matrix is a function of the Lamé parameters, λ and μ and a normal and tangential fracture compliance, Z_N and Z_T respectively. For a set of fractures in the x_2-x_3 plane, the effective elastic compliance matrix is given by

$$\underline{\underline{S}} = \begin{bmatrix} \frac{\lambda+\mu}{\mu(3\lambda+2\mu)} + Z_N & -\frac{\lambda}{2\mu(3\lambda+2\mu)} & -\frac{\lambda}{2\mu(3\lambda+2\mu)} & 0 & 0 & 0 \\ -\frac{\lambda}{2\mu(3\lambda+2\mu)} & \frac{\lambda+\mu}{\mu(3\lambda+2\mu)} & -\frac{\lambda}{2\mu(3\lambda+2\mu)} & 0 & 0 & 0 \\ -\frac{\lambda}{2\mu(3\lambda+2\mu)} & -\frac{\lambda}{2\mu(3\lambda+2\mu)} & \frac{\lambda+\mu}{\mu(3\lambda+2\mu)} & 0 & 0 & 0 \\ 0 & 0 & 0 & \frac{1}{\mu} & 0 & 0 \\ 0 & 0 & 0 & 0 & \frac{1}{\mu}+Z_T & 0 \\ 0 & 0 & 0 & 0 & 0 & \frac{1}{\mu}+Z_T \end{bmatrix} ,$$
(A-7)

with the corresponding inverse or elastic stiffness matrix given by

$$\underline{\underline{A}}^n = \begin{bmatrix} \dfrac{M}{\rho}(1-\delta_N) & \dfrac{\lambda}{\rho}(1-\delta_N) & \dfrac{\lambda}{\rho}(1-\delta_N) & 0 & 0 & 0 \\[2mm] \dfrac{\lambda}{\rho}(1-\delta_N) & \dfrac{M}{\rho}(1-r^2\delta_N) & \dfrac{\lambda}{\rho}(1-r\delta_N) & 0 & 0 & 0 \\[2mm] \dfrac{\lambda}{\rho}(1-\delta_N) & \dfrac{\lambda}{\rho}(1-r\delta_N) & \dfrac{M}{\rho}(1-r^2\delta_N) & 0 & 0 & 0 \\[2mm] 0 & 0 & 0 & \dfrac{\mu}{\rho} & 0 & 0 \\[2mm] 0 & 0 & 0 & 0 & \dfrac{\mu}{\rho}(1-\delta_T) & 0 \\[2mm] 0 & 0 & 0 & 0 & 0 & \dfrac{\mu}{\rho}(1-\delta_T) \end{bmatrix}, \qquad \text{(A-8)}$$

where

$$M = \lambda + 2\mu, \qquad\qquad\qquad \text{(A-9)}$$

$$r = \frac{\lambda}{M}, \qquad\qquad\qquad \text{(A-10)}$$

$$\delta_T = \frac{Z_T\mu}{1+Z_T\mu}, \qquad\qquad\qquad \text{(A-11)}$$

and

$$\delta_N = \frac{Z_N M}{1+Z_N M}. \qquad\qquad\qquad \text{(A-12)}$$

APPENDIX B

Static moduli

The components of the static Poisson's ratio for an orthorhombic medium in terms of the elastic stiffness parameters are given by

$$\nu_{12} = \frac{C_{23}C_{13} - C_{12}C_{33}}{C_{22}C_{33} - C_{23}^2}, \tag{B-1}$$

$$\nu_{13} = \frac{C_{12}C_{23} - C_{22}C_{13}}{C_{22}C_{33} - C_{23}^2}, \tag{B-2}$$

$$\nu_{21} = \frac{C_{23}C_{13} - C_{12}C_{33}}{C_{11}C_{33} - C_{13}^2}, \tag{B-3}$$

$$\nu_{23} = \frac{C_{12}C_{13} - C_{11}C_{23}}{C_{11}C_{33} - C_{13}^2}, \tag{B-4}$$

$$\nu_{31} = \frac{C_{12}C_{23} - C_{22}C_{13}}{C_{11}C_{22} - C_{12}^2}, \tag{B-5}$$

and

$$\nu_{32} = \frac{C_{12}C_{13} - C_{11}C_{23}}{C_{11}C_{22} - C_{12}^2}, \tag{B-6}$$

and the components of the static Young's modulus are given by

$$E_1 = \frac{D}{C_{22}C_{33} - C_{23}^2}, \tag{B-7}$$

$$E_2 = \frac{D}{C_{11}C_{33} - C_{13}^2}, \tag{B-8}$$

and

$$E_3 = \frac{D}{C_{11}C_{22} - C_{12}^2} \, , \tag{B-9}$$

where

$$D = \det \begin{vmatrix} C_{11} & C_{12} & C_{13} \\ C_{12} & C_{22} & C_{23} \\ C_{13} & C_{23} & C_{33} \end{vmatrix} . \tag{B-10}$$

The static moduli are functions of only C_{11}, C_{22}, C_{33}, C_{12}, C_{13}, and C_{23} and are independent of the elastic stiffness parameters associated with the S-wave propagation velocities.

References

Aarre, V., Astratti, D., Dayyni, T. N. A. A., Mahmoud, S. L., Clark, A. B. S., Stellas, M. J., Stringer, J. W., Toelle, B., Vejbaek, O. V., and White, G., 2012, Seismic detection of subtle faults and fractures: Oilfield Review, Schlumberger, **24**, no.2, 28-43.

Aki, K., and Richards, P. G., 1980, Quantitative seismology: W.H. Freeman & Co.

Auld, B. A., 1990, Acoustic fields and waves in solids: Krieger Pub Co.

Biot, M. A. and Willis, D. G., 1957, The elastic coefficients of the theory of consolidation: Journal of Applied Mechanics, **24**, 594-604.

Bond, W., 1943, The mathematics of the physical properties of crystals: BSTJ, **22**, 1-72.

Brajanovski, M., Gurevich, B., and Schoenberg, M., 2005, A model for P-wave attenuation and dispersion in a porous medium permeated by aligned fractures: Geophys. J. Int., **163**, 372-384.

Chopra, S., and Marfurt, K., 2007, Seismic attributes for prospect identification and reservoir characterization: Society of Exploration Geophysicists, Tulsa.

Cipolla, C. L., Williams, M. J., Weng, X, Mack, M., and Maxwell, S., 2010, Hydraulic fracture monitoring to reservoir simulation: Maximizing value: SPE Annual Technical Conference and Exhibition, Florence, Italy, SPE-133877.

Coulomb, C. A., 1773, Application of the rules of maxima and minima to some problems of statics related to architecture: Acad. Roy. Sci. Mem. Math. Phys., **7**, 343-382.

Crampin, S., 1987, Geological and industrial implications of extensive-dilatancy anisotropy: Nature, **328**, 491-496.

Daley, P. F., and E. Krebes, 2006, Quasi-compressional group velocity approximation in a weakly anisotropic orthorhombic medium: Journal of Seismic Exploration, **14**, 319-334.

Downton, J., and Roure, B., 2010, Azimuthal simultaneous elastic inversion for fracture detection: 80th Annual International Meeting, SEG, Expanded Abstracts, 263-267.

Duchane D., and Brown, D., 2002, Hot dry rock (HDR) geothermal energy research and development at Fenton Hill, New Mexico: GHC Bulletin, **23**, no. 4, 13-19.

Eisner, L., Janská, E., Opršal, I., and Matoušek, P., 2011, Seismic analysis of the events in the vicinity of the Preese Hall well: Report from Seismik to Cuadrilla Resources.

Engelder, T., and Lacazette, A., 1990, Natural hydraulic fracturing: Rock Joints (ed. Barton, N., and Stephansson, O.), A. A. Balkema, Brookfield, 35-44.

Engelder, T., and Fischer, M. P., 1996, Loading configurations and driving mechanisms for joints based on Griffith energy-balance concept: Tectonophysics, **256**, 253-277.

English, J. M., 2012, Thermomechanical origin of regional fracture systems: AAPG Bulletin, **96**, no. 9, 1597-1625.

Florez-Niño, J. M., Aydin, A., Mavko, G., Antonellini, M., and Ayaviri, A., 2005, Fault and fracture systems in a fold and thrust belt: An example from Bolivia: AAPG Bulletin, **89**, no. 4, 471-493.

Fraser, K., and O. Catuneanu, 2004, Sedimentology and geochemistry of the Second White Specks Formation, North/Central Alberta, Canada: CSPG, Annual Convention Abstracts.

Gabrielse, H., and C. J. Yorath, 1991, Geology of the Cordilleran Orogen in Canada: Geological Survey of Canada, Geology of Canada, **4**, 3-11.

Goodway, B., Monk, D., Perez, M., Purdue, G., Anderson, P., Iverson, A., Vera, V., and Cho, D., 2012, Combined microseismic and 4D to calibrate and confirm surface 3D AVO/LMR predictions of completions performance and well production in the Horn River gas shales of NEBC: The Leading Edge, **31**, no. 12, 1502-1511.

Griffith, A. A., 1920, The phenomena of flow and rupture in solids: Phil. Trans. Roy. Soc. Lond. Ser. A, **221**, 163-198.

Gurevich, B., Galvin, R. J., Brajanovski, M., Müller, T. M., and Lambert, G., 2007, Fluid substitution, dispersion, and attenuation in fractured and porous reservoirs – insights from new rock physics models: The Leading Edge, **26**, no. 9, 1162-1168.

Gutenberg, B., and Richter, C. F., 1954, Seismicity of the Earth and associated phenomena: 2nd ed., Princeton University Press.

Hallbauer, D. K., Wagner, H., and Cook, N. G. W., 1973, Some observations concerning the microscopic and mechanical behavior of quartzite specimens in stiff triaxial compression tests: Int. J. Rock Mech., **10**, 713-26.

Holland, A., 2011, Examination of possibly induced seismicity from hydraulic fracturing in the Eola Field, Garvin County, Oklahoma: Oklahoma Geological Survey Open-File Report OF1-2011.

Hubbert, M. K., 1956, Nuclear energy and the fossil fuels: American Petroleum Institute Conference, San Antonio, Texas.

Hudson, J. A., 1981, Wave speeds and attenuation of elastic waves in material containing cracks: Geophysical Journal of the Royal Astronomical Society, **64**, 133-150.

Innanen, K. A., 2012, AVO theory for large contrast elastic and anelastic targets in pre-critical regimes: SEG Expanded Abstracts.

Jaeger, J. C., Cook, N. W. G., and Zimmerman, R. W., 2007, Fundamentals of Rock Mechanics: 4th ed., Blackwell Publishing.

Jenner, E., 2002, Azimuthal AVO: Methodology and data examples, The Leading Edge, **21**, no. 8, 782-786.

Judd, W. R., 1964, Rock stress, rock mechanics and research, in state of stress in the Earth's crust, W. R. Judd, ed., Elsevier, New York, 5-51.

Kolmogorov, A. N., Petrovskii, I. G., and Piskunov, N. S., 1937, A study of the diffusion equation with increase in the quantity of matter, and its application to a biological problem: Bull. Moscow Univ. Math. ser. A1, 1-25.

Kraft, T., Mai, P. M., Wiemer, S., Deichmann, N., Ripperger, J., Kästli, P., Bachmann, C., Fäh, D., Wössner, J., and Giardini, D., 2009, Enhanced geothermal systems: Mitigating risk in urban areas: EOS, **90**, no. 32, 273-274.

Lacazette, A., and Engelder, T., 1992, Fluid-driven cyclic propagation of a joint in the Ithaca Siltstone, Appalachian Basin, New York: Fault mechanics and transport properties of rocks (ed. Evans, B., and Wong, T. F.), 297-323.

Lacazette, A., 2000, Natural fracture nomenclature, Disk 1, 13 pages, in L.B. Thompson (editor), Atlas of borehole images, AAPG Datapages Discovery Series 4, American Association of Petroleum Geologists, Tulsa (2 compact disks).

Lacazette, A., 2009, Natural fracture nomenclature, in L.B. Thompson (editor) Atlas of borehole images, Second edition, AAPG Datapages Discovery Series 4, American Association of Petroleum Geologists (compact disks).

Lee, J., Spivey, J. P., and Rollins, J. B., 2003, Pressure transient testing: SPE Textbook Series vol. 9.

Maxwell, S. C., Waltman, C. K., Warpinski, N. R., Mayerhofer, M. J., and Boroumand, N., 2006, Imaging seismic deformation associated with hydraulic fracture complexity: SPE Annual Technical Conference and Exhibition, San Antonio, Texas, SPE 102801.

Maxwell, S. C., Jones, M., Parker, R., Miong, S., Leaney, S., Dorval, D., D'Amico, D., Logel, J., Anderson, E., and Hammermaster, K., 2009, Fault Activation During Hydraulic Fracturing: SEG Expanded Abstracts.

Maxwell, S. C., Cho, D., Pope, T., Jones, M., Cipolla, C., Mack, M., Henery, F., Norton, M., 2011, Enhanced reservoir characterization using hydraulic fracture microseismicity: SPE Hydraulic Fracturing Technology Conference and Exhibition, The Woodlands, Texas, SPE 140449.

Metropolis, N., Rosenbluth, A., Rosenbluth, M., Teller, A., and Teller, E., 1953, Equation of state calculations by fast computing machines: J. Chem. Phys., **21**, 1087-1092.

Norton, M., Hovdebo, W., Cho, D., Jones, M., and Maxwell, S., 2010, Surface seismic to microseismic: An integrated case study from exploration to completion in the Montney Shale, NE British Columbia, Canada: SEG Expanded Abstracts.

Pedersen, S. I., Randen, T., Sønneland, L., and Steen, Ø., 2002, Automatic fault extraction using artificial ants: SEG Expanded Abstracts.

Potter, R. M., Robinson, E. S., and Smith M. C., 1974, Method of extracting heat from dry geothermal reservoirs: US Patent #3786858.

Pšenčík, I., and Martins, J. L., 2001, Properties of weak contrast PP reflection/transmission coefficients for weakly anisotropic elastic media: Studia geoph. et geod. **45**, 176-199.

Rothman, D. H., 1985, Nonlinear inversion, statistical mechanics and residual statics estimation: Geophysics, **50**, 2784-2796.

Rüger, A., and Tsvankin, I., 1997, Using AVO for fracture detection: Analytic basis and practical solutions: The Leading Edge, **16**, no. 10, 1429-1434.

Rüger, A., 1998, Variation of P-wave reflectivity with offset and azimuth in anisotropic media: Geophysics, **63**, no. 3, 935-947.

Rutledge, J. T., Phillips, W. S, and Mayerhofer, M. J., 2004, Faulting induced by forced fluid injection and fluid flow forced by faulting: An interpretation of hydraulic-fracture microseismicity, Carthage Cotton Valley gas field, Texas: Bulletin of Seismological Society of America, **94**, 1817-1830.

Sack, R. A., 1946, Extension of Griffith's theory of rupture to three dimensions: Proc. Phys. Soc. London, **58**, 729-36.

Salvini, F., and Storti, F., 2001, The distribution of deformation in parallel fault-related folds with migrating axial surfaces: Comparison between fault-propagation and fault-bend folding: Journal of Structural Geology, **23**, no. 1, 25-32.

Sayers, C. M., 2010, Geophysics under stress: Geomechanical applications of seismic and borehole acoustic waves: SEG/EAGE Distinguished Instructor Series, no. 13.

Schoenberg, M., and C. Sayers, 1995, Seismic anisotropy of fractured rock: Geophysics, **60**, 204–211.

Sen, M. K., Stoffa, P. L., 1991, Nonlinear one-dimensional seismic waveform inversion using simulated annealing: Geophysics, **56**, 1624-1638.

Shemeta, J. E., Eide, E. A., Hitzman, M. W., Clarke, D. D., Detournay, E., Dieterich, J. H., Dillion, D. K., Green, S. J., Habiger, R. M., McGuire, R. K., Mitchell, J. K.,

Smith, J. L., Ortego, J. R., and Gibbs, C. R., 2012, The potential for induced seismicity in energy technologies: The Leading Edge, **31**, no.12, 1438-1444.

Sheriff, R. E., and Geldarrt, L. P., 1995, Exploration Seismology: Cambridge University Press.

Sneddon, I. N., 1946, The distribution of stress in the neighborhood of a crack in an elastic solid: Proc. Roy. Soc. Lond. Ser. A, **187**, 229-60.

Suppe, J., 1983, Geometry and kinematics of fault-bend folding: American Journal of Science, **283**, 684-721.

Thomsen, L., 1993, Weak anisotropic reflections, *in* Castagna, J. P., and Backus, M. M., Eds., Offset-dependent reflectivity – Theory and practice of AVO analysis: SEG, 103-111.

Vavryčuk, V., and Pšenčík, I., 1998, PP-wave reflection coefficients in weakly anisotropic elastic media: Geophysics, **63**, 2129-2141.

Warpinski, N. R., Du, J., and Zimmer, U., 2012, Measurements of hydraulic-fracture-induced seismicity in gas shales: SPE Hydraulic Fracturing Technology Conference, The Woodlands, Texas, USA, SPE-151597.

Yost II, A. B., Carden, R., Muncey, J. G., Stover, W. E., and Scheper, R. J., 1990, Air drilling and multiple hydraulic fracturing of a 72 degree slant well in Devonian shale: SPE Eastern Regional Meeting, Columbus, Ohio, SPE 21264.

Zoback, M. D., Kohli, A., Das, I., and McClure, M., 2012, The importance of slow slip on faults during hydraulic fracturing stimulation of shale gas reservoirs: SPE Americas Unconventional Resources Conference, Pittsburgh, Pennsylvania, SPE 155476.